Additive Manufacturing 98 (2025) 104636

Contents lists available at ScienceDirect

Additive Manufacturing

journal homepage: www.elsevier.com/locate/addma

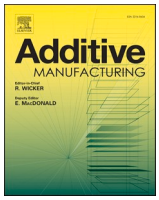

Material extrusion 3D printing of bioactive smart scaffolds for bone tissue engineering

Nasim Sabahi [a], Iman Roohani [b], Chun H. Wang [a], Xiaopeng Li [a,*]

[a] School of Mechanical and Manufacturing Engineering, The University of New South Wales (UNSW Sydney), Sydney, NSW 2052, Australia
[b] Tissue Engineering and Biomaterials Research Unit, School of Biomedical Engineering, The University of Sydney, Sydney, NSW 2006, Australia

ARTICLE INFO

Keywords:
Material extrusion
Shape-memory scaffold
Shape-memory filament
Shape recovery
Polydopamine coating

ABSTRACT

3D printing of smart scaffolds, based on material extrusion-based additive manufacturing techniques, offers a novel solution for the treatment of irregular bone defects using minimally invasive techniques. However, the progress of this approach has been hindered by the lack of printable shape-memory materials and functional biomedical scaffolds that exhibit high shape recovery and closely match the core properties of human bone. Herein, we present the 3D printing of novel bioactive smart scaffolds with tunable architecture, mechanical properties, and shape memory performance. To achieve this, we developed a thermo-responsive biocompatible shape memory filament comprising poly (ε-caprolactone) and thermoplastic polyurethane, specifically tailored for material extrusion 3D printing. Careful printability assessment of the smart filament enabled successful 3D printing of scaffolds with diverse densities, pore geometries, and architectures. The scaffolds were also functionalized with a bioactive polydopamine (PDA) coating to enhance their hydrophilicity and cytocompatibility without compromising their mechanical and shape memory performance. Thermomechanical cyclic tests demonstrated that the shape fixity, shape recovery, and transition temperature of programmed scaffolds can be tailored by controlling scaffold architecture and density. The scaffolds with gyroid, rectilinear, and triangular architecture and 50 % infill density exhibited excellent shape recovery performance at the transition temperature of 52°C, achieving shape recovery percentages of 98 %, 91.1 %, and 89.5 %, respectively. Additionally, all scaffolds exhibited rapid recovery, with a maximum response time of 180 seconds. MG-63 cell evaluation confirmed the bioactivity and cytocompatibility of both untreated and PDA-treated scaffolds, with the PDA-coated scaffolds showing improved proliferation and biomineralization.

1. Introduction

Bone is among the human organs capable of natural self-healing after injury, all without the formation of scars [1]. However, despite this incredible natural regenerative potential, bone healing remains a complex challenge in clinical practice. Autograft remains the preferred technique for repairing bone; however, it has drawbacks such as limited availability, high risk of infection, and second-site morbidity [2]. Meanwhile, synthetic solutions like bone grafts come in either particulate forms or prefabricated static three-dimensional scaffolds, lacking the ability to actively change their shape and adapt to the boundaries of irregular-shaped bone defects. This poses a significant challenge when treating and reconstructing such complex defects [3–5].

In recent years, 4D printing has emerged as a promising solution for treating irregular bone defects. This innovative approach combines 3D printing technology with shape memory polymers (SMPs) to create smart scaffolds that can dynamically transform into complex and adaptive structures over time [6,7]. 4D-printed smart scaffolds have the

Abbreviations: AM, Additive Manufacturing; FDM, Fused Deposition Modeling; EM, Extrusion Multiplier; BDO, 1,4-Butanediol; CaP, Calcium Phosphate; CNT, Carbon Nanotube; DA, Dopamine Hydrochloride; PDA, Polydopamine; DMEM, Dulbecco's Modified Eagle's Medium; FBS, Fetal Bovine Serum; DSC, Differential Scanning Calorimetry; EDS, Energy Dispersive Spectrometer; XRD, X-ray Diffraction; FTIR, Fourier Transform Infrared Spectroscopy; MDI, Methylene Diphenyl Diisocyanate; MG-63, Osteoblast-like cell line derived from human osteosarcoma; MTS, 3–4,5-dimethylthiazol-2-yl-5–3-carboxymethoxyphenyl-2H-tetrazolium; PCL, Polycaprolactone; PLA, Polylactic Acid; TPU, Thermoplastic Polyurethane; CAD, Computer-Aided Design; HA, Hydroxyapatite; PELA, Polyd,l-lactic acid-co-ethylene glycol-co-d,l-lactic acid; SMP, Shape Memory Polymer; SEM, Scanning Electron Microscopy; TGA, Thermogravimetric Analysis; TPMS, Triply Periodic Minimal Surface; Ttrans, Transition Temperature; PVC, Polyvinyl chloride.

* Corresponding author.
E-mail address: xiaopeng.li@unsw.edu.au (X. Li).

https://doi.org/10.1016/j.addma.2024.104636
Received 27 March 2024; Received in revised form 12 December 2024; Accepted 30 December 2024
Available online 2 January 2025

remarkable ability to change their shape and size in response to an external stimulus such as temperature, allowing them to conform more precisely to the irregular contours of bone defects. Furthermore, this distinctive feature enables these scaffolds to be compressed before in vivo implantation, making them suitable for minimally invasive surgical procedures. Upon insertion, they undergo a dynamic response, effectively restoring their complex original shape, allowing them to fill the defect area (Fig. 1). By facilitating better integration with the surrounding tissues, this innovative approach can significantly enhance the success rate and efficacy of bone tissue regeneration, ultimately leading to better clinical outcomes for patients [8].

Thermo-responsive shape memory scaffolds can be reshaped and compacted into a temporarily stable shape according to the requirement and return to their initial shape when exposed to an external thermal field. Achieving this temporary shape involves deforming the shape memory scaffold at a temperature below the transition temperature (T_{trans}) of shape memory material when the mobility of molecular chain segments is limited. At this stage, a substantial quantity of elastic energy is retained within the programmed shape memory scaffold, serving as the impetus for restoring the initial shape. Molecular mobility is reactivated when the shape memory scaffold is once again heated above T_{trans}, prompting the polymer chains to return to their higher entropy structural configuration. Consequently, the polymeric scaffold reassumes its original shape. The transformation temperature could be either the temperature at which the material melts (T_m) or the temperature at which it undergoes a glass transition (T_g) in the switching segment of SMP [9].

Extrusion 3D printing methods, including Fused Deposition Modelling (FDM), are among the various 3D printing technologies used to produce patient-specific polymeric bone scaffolds [9]. FDM is a filament-based 3D printing technology that uses the melt extrusion method to selectively deposit thermoplastic filament layer-by-layer according to a CAD design. FDM offers a solvent-free, fast, and cost-effective method for creating customized, high-quality scaffolds that meet specific patient needs. The materials utilized in FDM printing include thermoplastic polymers and polymer composites. Recently, there have been a few developments in the field of shape memory filaments for FDM printing. These filaments include thermoplastic polyurethane/ polylactide (TPU/PLA) blends at ratios of 5:5, 7:3, and 9:1 [10], as well as 1:9, 1:4, 3:7, and 2:3 wt% ratios [11]. Other filaments include polycaprolactone (PCL)/PLA at composition ratios of 3:1, 2:1, and 1:1 [12], PCL/TPU at a 7:3 wt% ratio [13], Polyvinyl chloride (PVC)/PCL at a 9:1 and 9.5:0.5 wt% ratio [14], and polybutylene succinate (PBS)/PLA at a 9:1 wt% ratio [15]. Additionally, several composite filaments have been developed, such as PLA/Fe_3O_4 [16], TPU/CNT [17], and PLA/CNT [18]. However, it is important to note that these filaments have not been specifically designed for healthcare applications, such as tissue engineering, where both biocompatibility and mechanical performance are essential. In particular, scaffolds printed with these filaments must provide the necessary compressive strength, elastic modulus, shape memory performance, and porosity to effectively mimic the mechanical properties of natural bone for successful tissue regeneration. Despite their potential, there are still limited studies on smart scaffolds fabricated using FDM printing.

In a study by Senatov et al., FDM printing was utilized to create porous scaffolds using PLA and a PLA/15 wt% hydroxyapatite (HA) composite, with an average pore size of 700 μm and porosity of 30 vol%. The primary objective was to investigate the influence of HA particles on the shape memory properties of the composite scaffolds. Their findings revealed that PLA/15 wt% HA scaffolds exhibited quicker development of recovery stresses, with the highest recovery stress of 3.0 MPa reached at a temperature of 70 °C. The dispersed HA particles played a role as nucleation centers, adding additional rigid phases that constrained molecular mobility. Consequently, the transition temperature of the composite scaffold shifted from 53 to 57°C [19–21]. Kutikov et al. [22] conducted a study where they synthesized and created poly(d,l-lactic acid-*co*-ethylene glycol-*co*-*d*,l-lactic acid) (PELA) and PELA/HA filaments for FDM printing of porous scaffolds. The researchers reported that the developed filaments had a transition temperature of T_{Trans} = 50°C and exhibited a shape recovery rate of over 90 %. Zhou et al. [23] prepared PLA/Fe_3O_4 shape memory scaffolds using 4D FDM printing technology, which were then coated with bioactive HA nanoparticles to promote bone tissue regeneration. The SMP scaffolds they developed displayed shape memory properties upon exposure to a magnetic field. In another study, Yousefi et al. [24] created multifunctional PLA/PBAT/Fe_3O_4 nanocomposites for 4D printing, optimized with 10 wt% Fe3O4. These materials showed enhanced toughness, thermal stability, and rapid shape-memory responses under thermal and magnetic activation, offering significant potential for remote-controlled tissue engineering applications.

The development of new printable bioactive smart filaments compatible with FDM printing is crucial for advancing bone tissue engineering [25]. Furthermore, it is important to understand how to optimize the FDM printing process and scaffold characteristics to achieve precise control over the shape memory performance of 4D printed constructs. This optimization is essential to ensure easy implantation and promote rapid, enhanced recovery when filling critical-sized bone defects. Additionally, evaluating the biocompatibility of developed shape memory filaments and 4D printed scaffolds is essential to determine their bioactivity and tissue compatibility for their successful

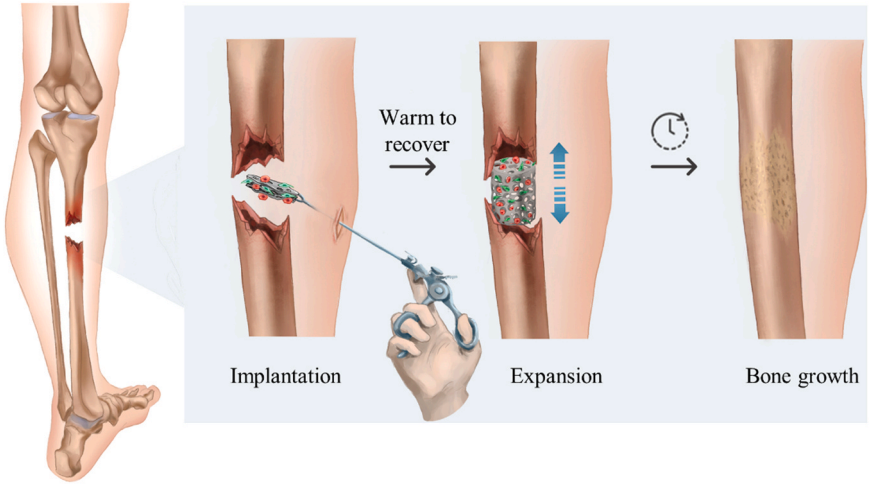

Fig. 1. Schematic representation of minimally invasive implantation of a compacted shape memory scaffold pre-seeded with cells and growth factors.

application in bone tissue engineering.

The primary objective of this study is to advance FDM 4D printing technology to develop smart scaffolds with optimal shape memory properties, while also possessing structural and functional similarities to cancellous bone. By optimal shape memory properties, this study refers to the scaffold's ability to fix a temporary shape during deformation and efficiently recover its original shape upon exposure to a stimulus, such as heat. These properties are critical for ensuring minimally invasive implantation and promoting accurate, full recovery of the scaffold to fill bone defects. Achieving this requires balancing shape fixity and shape recovery ratios within biocompatible temperature ranges, making the scaffolds highly suitable for in vivo applications. To achieve this, firstly, a novel shape memory filament was created using a blend of 70 wt% amorphous TPU and 30 wt% semi-crystalline PCL, selected based on previous studies demonstrating their suitability for shape memory performance with the lowest transition temperature observed in TPU/PCL blends when the PCL is blended with a higher amount of TPU [9,26,27]. This careful selection allows the development of shape memory scaffolds that can safely activate in a temperature range suitable for the body, respond to their environment, and promote tissue regeneration. The printability, physiochemical properties, and morphology of the filament were extensively evaluated both before and after extrusion to assess the impact of the FDM printing technique on the printability of the developed filament. Following this, the shape memory filament was used to 4D print porous scaffolds with varying pore architecture and porosities. The intention was to investigate the influence of FDM printing parameters and scaffold architecture on the morphology, mechanical properties, and shape memory performance of the scaffolds. In addition, polydopamine, a bioactive substance, was used to coat the pore walls of FDM printed shape memory scaffolds, and the hydrophilicity and cytocompatibility of both uncoated and coated scaffolds were assessed using the MTS assay (3-(4,5-dimethylthiazol-2-yl)-5-(3-carboxymethoxyphenyl)-2-(4-sulfophenyl)-2H-tetrazolium assay) and MG-63 osteoblast-like cells (derived from a human osteosarcoma cell line). The findings of this study highlight the potential of the new shape memory scaffolds we developed using FDM 4D printing technology, particularly when coupled with bioactive coatings, as a promising solution for tissue engineering applications.

2. Experimental

2.1. Materials

Polycaprolactone (PCL) was purchased from BOC Science Co. with a melting point of 58°C and a density of 1.14 g/cm^3. TPU with a density of 1.21 g/cm^3 was also obtained from Redox Plastics (Ellastolan) Co. The TPU utilized in the present study is a Thermoplastic Polyester-Polyurethane. The soft segment is based on an adipic acid-based polyester polyol, and the hard segment is derived from 4,4′-MDI and 1,4-Butanediol (BDO). Tris(hydroxymethyl)aminomethane and Dopamine hydrochloride were purchased from Sigma-Aldrich. Dulbecco's Modified Eagle's Medium (DMEM), Fetal bovine serum (FBS), L-glutamine, and penicillin-streptomycin were purchased from Invitrogen/Gibco Co. A CellTiter 96 Aqueous One Solution kit was purchased from Promega Co.

2.2. Filament fabrication

A TPU/PCL blend with a weight ratio of 70 % TPU and 30 % PCL was produced using a HAAKE Polylab QC twin-screw extruder. The resulting blend was labeled as "UC," with "C" indicating pure PCL and "U" signifying pure TPU. The mixing conditions were set at a screw speed of 100 rad min^{-1}, a temperature of 150°C, and a mixing period of 10 min. Fig. 1a shows the raw materials and molecular segments of the developed UC blend. After successful blend development, a printable shape memory filament was fabricated with a 3devo Composer 450 desktop filament maker (3D Evo B.V., Utrecht, The Netherlands). Firstly, the blended UC polymer was cut into granules, followed by drying in a vacuum oven for 3 h at 45°C. The 3devo filament maker is a single-screw extruder equipped with two cooling fans and four controllable heating zones, where heater 4 is at the feeding zone and heater 1 is close to the nozzle. The rotational speed of the extruder's screw was set to 5 rpm, and the fan's speed was set to 90 %. The heaters' (1 through 4) temperature was set to 190°C, 205°C, 210°C, and 200°C, respectively. Once all heaters reached the target temperatures, the dried pellets were placed in the hopper and the machine started extruding. Once the filament started coming out of the nozzle, it was led through a puller mechanism to keep the filament at a constant thickness. The UC filament with a diameter of 1.75 ± 0.05 mm was successfully fabricated to be used afterward in the FDM printing of porous shape memory scaffolds.

2.3. Printability assessment

To determine the accuracy of 3D printing using the fabricated UC filament, a printability assessment was performed. Parallelly arranged single lines of 20 mm length were designed on SLICER 4.0 software and were printed using an FDM printer (3DGence Once, Gliwice, Poland). The printing parameters in the Simplify3D software remained consistent, but the extrusion multiplier varied between 0.9 and 1.1, and the temperature varied between 200 and 220°C. The printed structures were analyzed using a phone camera and SEM imaging to evaluate the dimensional precision and morphology of the extruded filament. The optimal extrusion temperature and extrusion multiplier were selected based on extrudability, shape consistency and stability. Extrudability was considered good if no aggregates or other inhomogeneities were visible, the printed layers adhered properly to the bed table, and there was minimal bending or diameter deviation.

2.4. Scaffold design and fabrication

Firstly, SolidWorks software was used to design cubic 3D CAD models measuring 20 × 20 × 10 mm^3 (length × width × height), and then the CAD files were imported into SLICER 4.0 slicing software to slice the models into various lay-down patterns (Rectilinear, Triangular, Gyroid) with 20 %, 30 %, 40 %, and 50 % infill densities (i.e., 80, 70, 60, and 50 % porosity) [28]. A variable raster angle was used to create rectilinear and triangular patterns. Rectilinear and triangular designs were created using standard line infill but with different orientations. The rectilinear scaffolds were printed using a 0/90º raster angle, while the triangular scaffolds were printed using a 0/60º/120º raster angle. Gyroid scaffolds were printed using the gyroid infill available in the 3D model slicing software SLICER 4.0. Finally, UC filament was fed into an FDM 3D printer (3DGence Once, Gliwice, Poland) with a 0.4 mm nozzle, and porous scaffolds were printed. The printing parameters are listed in Table 1.

The layer height (0.2 mm) was selected based on the optimal ratio between nozzle diameter and layer height, which is typically 25–80 % of the nozzle diameter. The layer width (150 %) was chosen to improve interlayer adhesion, a critical factor for mechanical strength, particularly in scaffolds for bone regeneration where strong interlayer bonds

Table 1
Optimized FDM printing parameters for UC filament.

Parameter	Value
Nozzle diameter, mm	0.4
Primary layer height, mm	0.2
Layer width, %	150
Extruder temperature, °C	210
Print bed temperature, °C	70
Print speed, mm/min	500
Extrusion multiplier	1
Infill percentage, %	20, 30, 40, 50

prevent delamination. Print speed (500 mm/min) was optimized to balance print quality and efficiency. While faster speeds risk inaccuracies, this speed provided dimensional accuracy without significantly extending fabrication time. Finally, infill percentages (20–50 %) were chosen to tune porosity, essential for tissue ingrowth, while maintaining enough mechanical strength for load-bearing applications [29–31].

2.5. PDA surface treatment

Surface modification of FDM printed scaffolds was performed by immersing a rectilinear scaffold into 10 mM tris buffer solution (pH=8.5) with 2 mg mL^{-1} dopamine and stirring at 150 rpm for 16 h. Following that, the scaffold was thoroughly washed with deionized (DI) water and dried in a vacuum oven for 48 h at 45°C.

2.6. Cell culture and In vitro Cytocompatibility

The human osteoblast-like MG-63 cells (Passage 9, ATCC® CRL-1427 ™) were cultured in Dulbecco's Modified Eagle's Medium (DMEM) containing 10 % fetal bovine serum (FBS, Gibco), 2 mM L-glutamin, and 100 U/mL penicillin- 100 µg/mL streptomycin (Gibco)). Cells were sustained under a humidified atmosphere with 5 % CO2 at 37 °C. Media was changed every day to remove non-adherent cells and to ensure optimal conditions for cell growth. Subculturing was performed when cells reached 80 % confluence in a T-75 cell culture flask.

The MTS assay with the CellTiter 96 Aqueous One Solution kit from Promega Life Sciences was used to assess the cell proliferation and cytotoxicity of MG-63 cells on both untreated and PDA-treated scaffolds. First, all scaffolds were cut into disk-shaped samples, each with a diameter of 5 mm and a height of 1 mm. They were then sterilized through immersion in 75 % ethanol for 30 minutes. Subsequently, to ensure thorough sterilization, each side of the scaffold was exposed to UV light for a duration of 1 hour. Prior to seeding and to improve cell attachment, the scaffolds were then incubated overnight in the growth media. Following this, the growth media were carefully aspirated, and MG-63 cells were cultured in a 96-well plate at a density of 5000 cells per well. During the testing period on days 1, 3, and 7, the cells were treated with media containing 20 % MTS solution and incubated at 37°C for 1 hour. Afterward, 100 µL of the resulting media were transferred to a transparent 96-well plate, and the absorbance was measured at a wavelength of 490 nm. The statistical data is presented as mean ± standard deviation. Two-way ANOVA and Tukey's multiple tests were used for data analysis.

2.7. Characterization techniques

2.7.1. X-ray diffraction (XRD) analysis

X-ray diffraction (XRD) analysis was used to characterize the crystalline and amorphous phase of extruded filament. The analysis was conducted using an X-ray diffractometer (Aeris Research/Malvern Analytical) at 5 kV and 1000 mA. Experiments were conducted with a step size of 0.01 (2θ) within the range of 10° to 80°.

2.7.2. Differential scanning calorimetry (DSC)

Differential scanning calorimetry was applied to study the glass transition, melting temperature, and crystallization of the extruded filament using a NETZSCH DSC 204F1 Phoenix apparatus. Experiments were conducted within aluminum pans, carried out under a controlled nitrogen atmosphere. Each sample underwent a series of prescribed thermal cycles as follows: The samples were initially held at −70°C for 5 minutes, then heated at a constant rate of 10 °C/min until reaching 150°C, where it was maintained for 5 minutes for thermal equilibration. Subsequently, the samples were cooled down to −70°C at the same rate, followed by a 5-minute stabilization period at −70°C. Finally, a second heating cycle, again at 10 °C/min, brought the samples to 150°C, where they were held for an additional 5 minutes.

2.7.3. Morphology

The microstructure of the UC filament and the morphology, as well as the pore size of the FDM printed scaffolds were examined using scanning electron microscopy with the Hitachi 3400I SEM. SEM and X-ray energy dispersive spectrometer (EDS) mineral mapping techniques were also used to examine the morphology of the adhered cell, as well as to confirm the successful PDA coating, its homogenous dispersion, and the formation of biomineral structures during cell culture. The platinum coating of all samples, achieving a final thickness of 15 nm, was carried out using a Quorum Q300 model sputter coater with a sputter current of 30 mA.

2.7.4. Surface wettability

The surface wettability of the uncoated and PDA-coated SMP scaffolds was evaluated using the Theta Optical Tensiometer (Attension, Biolin Scientific). A sessile DI water droplet was carefully positioned on the surface of both uncoated and PDA-coated scaffolds, and a series of images capturing the droplet's spreading behavior over a 60-second interval were captured.

2.7.5. TGA

The thermogravimetric Analysis (TGA) measurement was conducted on the UC filament before and after FDM printing. The purpose of this analysis was to verify that the 3D printing temperature used in the study fell within the stable range of the material. The measurements were performed using a Netzsch TG 209 analyzer under a nitrogen (N2) atmosphere, with a heating rate of 10 °C/min, over a temperature range of 25°C to 600°C.

2.7.6. Mechanical behavior and shape memory performance of shape memory scaffolds

The mechanical properties of the 3D printed scaffolds were evaluated by compression test using a universal testing system (Instron testing machine 3369 model) equipped with a 10 kN load cell. In accordance with ASTM D695–15 standard, printed scaffolds (n = 3 per group) were compressed based on an 80 % deformation at a constant crosshead speed of 1 mm/min at room temperature. The scaffold surface area was measured prior to the mechanical assessment, and the slope of the straight-line portion of the stress-strain curve was used to calculate the compressive modulus.

To characterize the shape memory properties of the scaffolds, we conducted cyclic thermomechanical tests in compression mode using the same Instron testing machine equipped with an environmental chamber and a temperature controller. Liquid nitrogen was used as a cryogenic liquid during the experiments. The environmental chamber was securely attached to the Instron system's load frame, and the cyclic test was executed under displacement-controlled condition. Fig. 2 provided a schematic representation of the experimental process and illustrated all the stages involved in the shape memory test. The heating-cooling rate was 2 °C/min in each test and the strain rate of 0.5 mm/min was applied during all loading and unloading stages. At first a maximum compressive strain of 50 % was applied at 70°C (loading stage). It is noteworthy that even a minor increase in temperature above the activation point of a thermo-responsive shape memory polymer is adequate to trigger deformation [32]. Subsequently, the scaffolds were gradually cooled down to 25°C while maintaining the applied strain constant. Following a 30-minute equilibration period at this temperature, the load was carefully removed, reducing the stress on the specimens to zero (unloading phase). The stored strain and the shape fixity ratio (R_f) were recorded and calculated at this stage. As the final step in the experiment, the scaffold was heated to 70°C under stress-free condition, and the recovered strain (ε_p), and the shape recovery ratio (R_r) of scaffolds were measured and calculated [33]. The thermo-cyclic test was conducted three times for each scaffold to assess its repeatability and reliability. The shape fixity (R_f) and shape recovery ratio (R_r) are two key parameters to evaluate an SMP's capacity to preserve mechanical deformation

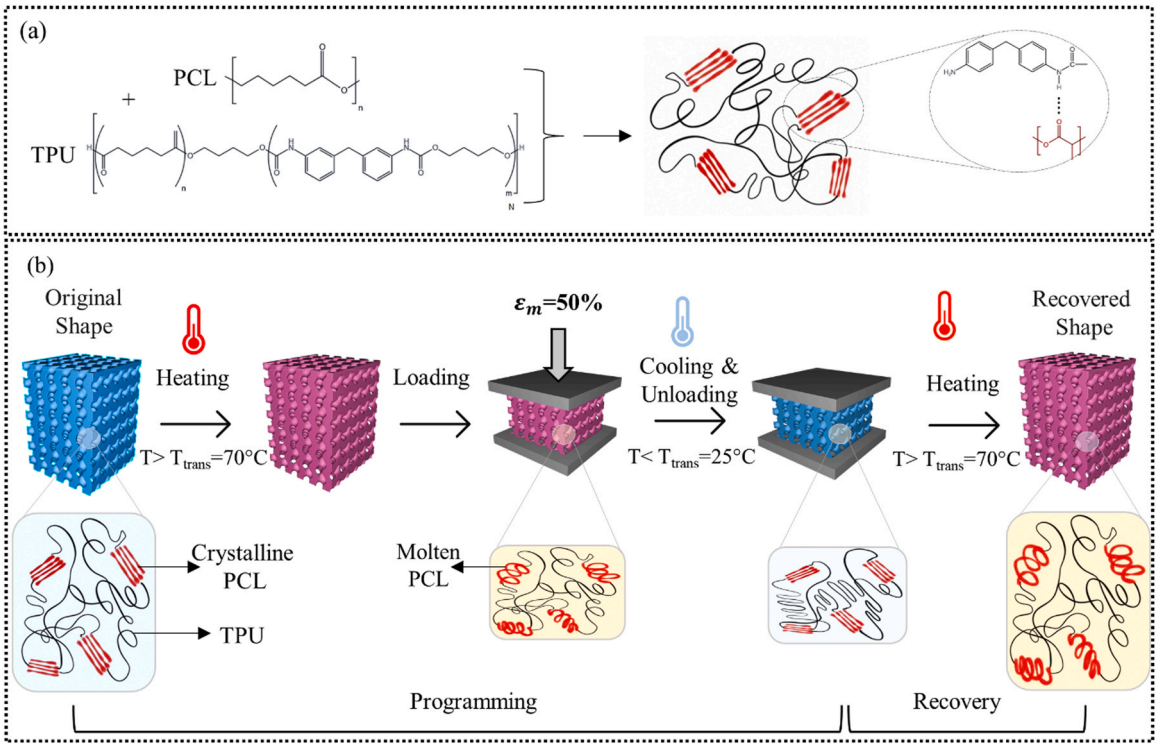

Fig. 2. (a) Raw materials and molecular segments of developed SMP, (b) A schematic depicting the experimental steps involved in programming and inducing shape recovery in SMP scaffolds, along with the molecular semi-crystalline scaffold transformations: Shape memory programming begins by initially raising the sample's temperature to 70°C, resulting in material softening and triggering increased mobility of polymer chains. Concurrently, the scaffold's temperature was kept at 70°C, while an external force was exerted to induce deformation. With the scaffold temperature still held at 70°C, an external load was applied to compress it. After this stage, and with the applied force sustained, the scaffold is gradually cooled down to 25°C (at this stage, the molecular chain segments solidify, leading to a lower-entropy state that becomes kinetically locked. This critical step results in the storage of a substantial quantity of elastic energy within the programmed shape memory scaffold, which serves as the impetus for recalling the initial shape). After unloading, the scaffold maintains its temporary shape, and when subjected to reheating at 70°C, the scaffold successfully undergoes shape recovery.

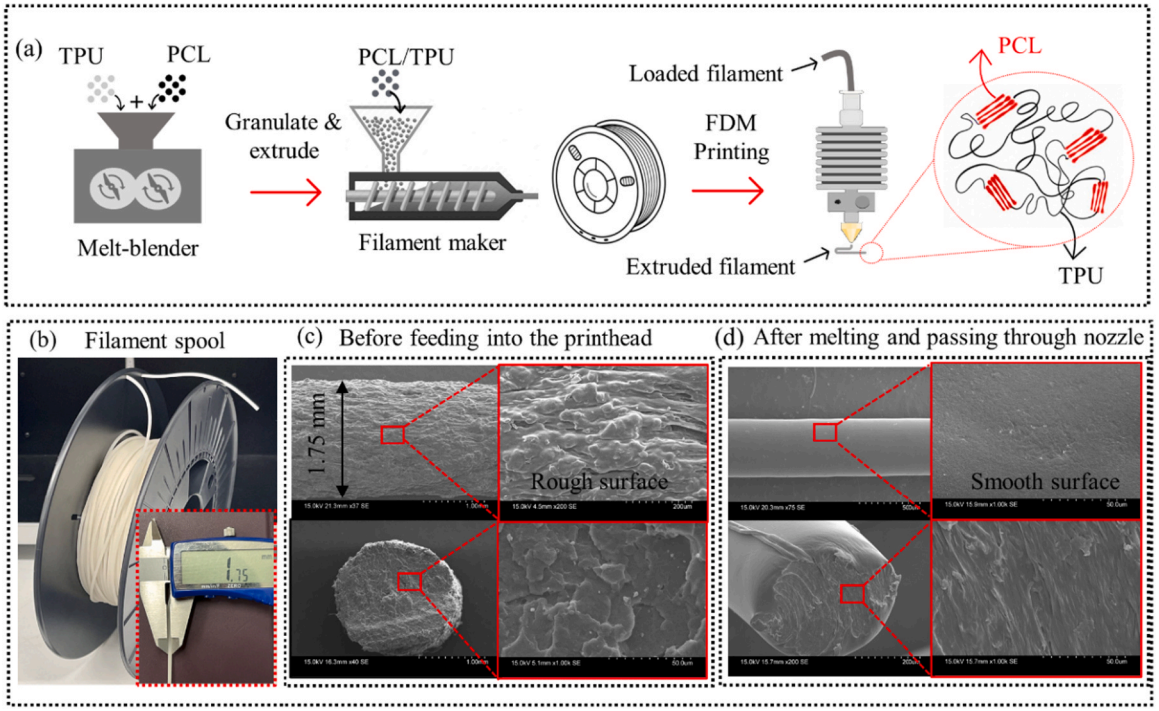

Fig. 3. (a) Schematic illustration of experimental steps involved in developing the UC shape memory filament for FDM printing technology. (b) Image of the final extruded UC filament with the aimed diameter of 1.75 mm. (c,d) SEM micrographs of the filament top surface and cross section prior and after FDM printing. The FDM extruding process had a significant impact on the physical properties of the filament, as evidenced by the markedly different morphology after printing.

and then return to its initial shape. These two parameters are defined as:

$$R_f = \varepsilon_u/\varepsilon_m \times 100 \quad (1)$$

$$R_r = \varepsilon_m - \varepsilon_p/\varepsilon_m \times 100 \quad (2)$$

3. Results and discussions

3.1. Filament production and characterization

Fig. 3a shows a schematic illustration of the 3D printing filament fabrication process, including blending TPU and PCL polymers in a twin-screw mixture followed by filament extrusion using a desktop extruder. Fig. 3b shows a spool of the final UC filament produced by this process. The diameter of the produced filament was measured with a digital caliper which was further confirmed using the SEM imaging technique. It was possible to produce UC filament with the aimed diameter (1.75 mm) suitable for FDM printing. UC blend contains two polymers that behave differently at high temperatures. One component is semi-crystalline PCL with a low melting temperature (58°C) and the other is amorphous TPU with a high extrusion melt temperature (150–220°C). During the extrusion process, the temperature of all heaters was kept around the processing temperature of TPU to get the appropriate flowability of the blend. The heaters' (1 through 4) temperature was set to 190°C, 205°C, 210°C, and 200°C, respectively. When the UC blend reaches the heaters' set temperature inside the extruder, the polymer chains become more flexible and form an amorphous structure, allowing the material to transform into viscous liquid through the melting process. Upon exiting the nozzle, the material rapidly cools down due to the considerable difference between the extruder's temperature and the lower ambient temperature. When the material undergoes rapid cooling, it spends only a brief period within the PCL crystallization temperature range. This rapid cooling, occurring briefly within the PCL crystallization temperature range, prevents the material from returning to its original crystalline structure. Instead, it solidifies in an amorphous state, resulting in uneven polymer shrinkage. To address this problem and ensure proper cooling of the output, a moderate rotation speed of 5 rpm was maintained for the filament maker's screw. This slower speed allowed the material to be extruded from the nozzle at a slower rate, enabling more time for effective cooling. Furthermore, to optimize the cooling process and promote efficient solidification, two external fans were strategically positioned near the nozzle, applying an external cooling rate of 90 %.

Fig. 3c and d also show the morphology of the cryogenic-fractured microstructure of the UC filament prior to and after FDM printing. Prior to FDM printing, the filament displayed a rough and heterogeneous morphology with dispersed tiny spherical phase domains. The surface of the filament appeared to be irregular, with no apparent boundaries. In 70TPU/30PCL %wt. polymer system, pure PCL creates a dispersed region, while TPU constitutes the continuous phase. In immiscible polymer blends, when the viscosity of the minor component (PCL) is less than that of the matrix, it will disperse within the matrix of the major component (TPU) [34]. However, after passing through the nozzle and melting during FDM printing, the filament exhibited a notably smoother surface with no obvious boundaries. This can be explained by the process of shear-induced orientation and flow alignment that occurs during the printing process. As the filament is extruded through the nozzle, it experiences shear forces that cause the polymer chains to align in the direction of flow, resulting in a more ordered and aligned structure. This can lead to a smoother surface and a reduction in phase separation. Additionally, the high temperature of the nozzle during printing can cause the surface of the filament to partially melt and fuse together, further smoothing the surface and reducing surface irregularities [35,36]. The resulting filament morphology after FDM printing was markedly different from its initial state, highlighting the significant impact of the FDM extruding process on the filament's physical properties.

We further characterized the crystallinity, thermal properties, and miscibility of the developed UC filament using XRD, DSC, TGA, and Fourier transform infrared (FTIR) spectroscopy techniques (Fig. 4). In physically cross-linked shape memory polymers, the shape fixity ratio in the polymer matrix is attributed to the crystalline phase, whereas the shape recovery ratio is influenced by the amorphous phase [9]. Hence, the presence of both crystalline and amorphous phases is a key requirement for a polymeric material to demonstrate shape memory characteristics. The XRD result of the UC filament proved the semi-crystalline nature of the developed material (Fig. 4a). In the case of UC polymer, two distinct crystallization peaks were detected at 21° and 24°, aligning with the diffraction patterns of the (110) and (200) lattice planes found in PCL polymer [37]. Nevertheless, when TPU was introduced into the blend, the intensities of these crystalline peaks diminished and became broader compared to pure PCL, indicating a reduced level of crystallinity in the UC blend in comparison to neat PCL. Overall, the XRD data suggests that the diffraction pattern results of the UC blend corresponded to the sum of the patterns for TPU and PCL, and both crystalline and amorphous phases exist. A DSC analysis was also performed on the extruded filament in the range of −70–150 to study the thermal properties, including glass transition, melting temperature, and crystallization of the extruded UC blend. During the initial heating process, it was observed that the melting temperature of pure PCL was 58°C, while the UC filament, which contains TPU, exhibited a reduced melting temperature of 52°C. This reduction suggests a decrease in crystallinity due to the TPU phase. However, during the second heating process, the diagram showed a melting temperature of 56°C, which is closer to the melting temperature of PCL. This suggests that the UC filament underwent some changes in its thermal properties during the first heating but returned closer to its original behavior during the second heating. On the other hand, the cold crystallization temperature (Tc) shifted to a higher temperature, rising from 27°C in neat PCL to 35°C in UC, accompanied by a reduction in crystallization enthalpy. The data suggest that the inclusion of TPU in the filament could hinder PCL crystallization, potentially negatively impacting the shape-fixing capabilities and avoiding achieving 100 percent shape fixity. This is because crystalline PCL serves as a crucial switching segment in the resulting UC shape memory filament [27].

The shape fixity of semicrystalline SMPs is significantly influenced by the material's crystallization potential. The crystallinity of a polymer blend can be obtained from DSC and analyzing the melting enthalpy data, which is directly correlated to the crystal content. Using Eq. 3, the crystallinity of samples was calculated.

$$X_c = \Delta H_m / w\Delta H^{\circ}_m \quad (3)$$

Where ΔH_m° is the heat of fusion of pure PCL, w represents the proportion of the second phase's weight in the blend, and ΔH_m is the heat of fusion of the UC blend.

The TGA data confirmed that the developed filament does not undergo thermal degradation at a temperature lower than 300°C. This indicates that the filament is stable and can be used reliably without the risk of degrading or breaking down at printing temperatures lower than 300°C. The FTIR spectroscopy results of pure polymers and developed filament are depicted in Fig. 4e. Pure TPU exhibited a distinct hydrogen-bonded N-H band at 3301 cm^{-1}, whereas the UC filament displayed an absorption peak corresponding to the free N-H band at 3335 cm^{-1}. The absorbance observed within the 1660–1780 range was assigned to the stretching vibration of C═O bands (amid I band). Notably, the peaks at 1695 and 1705 cm^{-1} are attributed to the stretching vibration of the carbonyl group within the hydrogen-bonded urethane groups of TPU. Further analysis of the UC filament's FTIR spectrum reveals a notable peak at 1720 cm^{-1}, which corresponded to the carbonyl group within the PCL content. We also examined the distinctive absorbances of the UC blend within the 1500–1550 cm^{-1} range. A peak was observed around

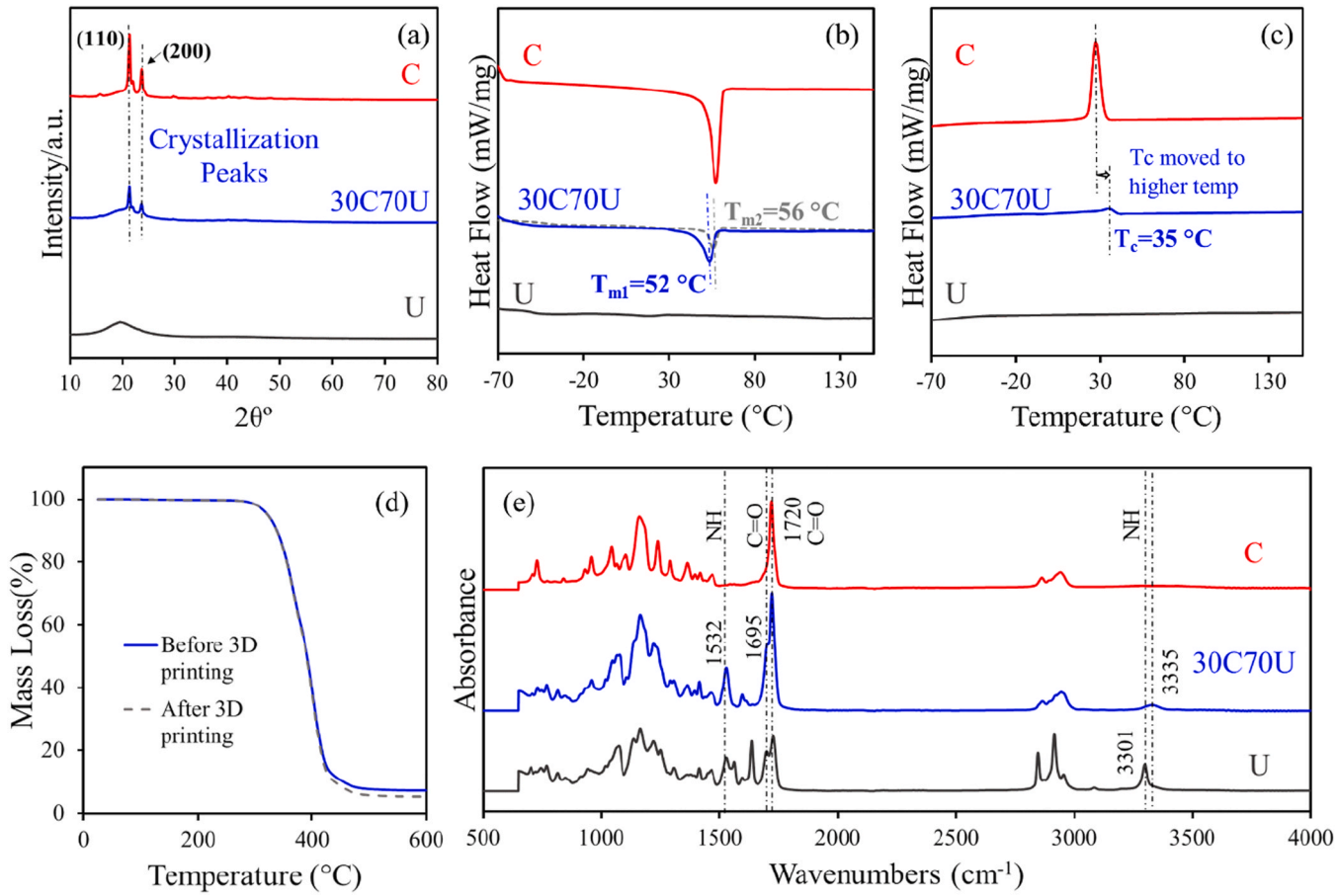

Fig. 4. (a) XRD diffraction pattern of neat PCL, neat TPU and developed UC blend, (b,c) DSC heating and cooling curves of PCL, TPU and UC polymer blend, (d) TGA analysis of developed filament prior and after 3D printing, (e) FTIR spectra of pure PCL, pure TPU and developed UC filament.

1532 and 1536 cm^{-1}, accompanied by a minor feature at 1512 cm^{-1}, corresponding to the bending vibrations of N-H groups within the urethane linkages of TPU. The FTIR results indicate the successful blending of two polymers, as the UC filament spectra exhibit a combination of the characteristic peaks of both the neat TPU and PCL. Table 2

3.2. Printability of UC filament

In extrusion-based AM techniques, the extrusion efficiency and 3D printed structure quality are highly dependent on the viscosity of the extruded filament as well as the amount of material extruded from the nozzle; hence the careful design of printing parameters, particularly nozzle temperature and extrusion multiplier (EM), is required to ensure consistent material flow and precise layer deposition [38]. The extrusion multiplier or extrusion flow rate controls the amount of material extruded from the nozzle. Inaccurate EM levels can lead to significant printing defects, including under-extrusion, over-extrusion, and dimensional inaccuracies, which can impact the final quality and functionality of the printed component [39,40]. To assess the printability of UC filament, parallelly arranged single lines of 20 mm length were designed (Fig. 5a) and printed.

The print speed, bed temperature, layer height and layer width were kept constants for all lines, but the extrusion multiplier and nozzle temperature varied between 0.9 and 1.1 and 190–220°C, respectively. As previously mentioned, the TGA results confirmed that the developed filament does not undergo thermal degradation at temperatures below 300°C. Therefore, the maximum printing temperature was set to 220°C. However, due to a noticeable decrease in print quality at temperatures above 220°C, no further tests were conducted at higher temperatures.

Fig. 5b shows the impact of nozzle temperature and extrusion multiplier on the extrudability, shape consistency and stability of printed structures. The figures with green, yellow, and red frames are described as “good quality”, “acceptable quality”, and “bad quality” prints, respectively. According to the results, the presence of non-stick layers was a significant issue when printing at a nozzle temperature of 190°C, as shown in Fig. 5b-1 to b-3. Non-stick layers occur when the printed material fails to adhere to the print bed, resulting in poor layer bonding, surface finish, and overall print quality. This problem could be resolved by increasing the nozzle temperature to promote better melting and flow characteristics of the material and improving interlayer adhesion [41]. Fig. 5b-4 and b-10 demonstrate an under-extrusion issue where small voids and gaps appear between the layers for the lines printed at an EM of 0.9, indicating insufficient material extrusion. However, increasing the extrusion flow rate to 100 % EM produced good quality lines at both print temperatures of 200 and 210°C, as shown in Fig. 5b-5 and b-8. Nevertheless, a wavy strut was observed in structures printed using an EM of 1.1, resulting from excessive extrusion of filament, as depicted in Fig. 5b-6, b-9, and e.

The under-extrusion issue observed in Fig. 5b-4 and b-10 can be attributed to a low extrusion flow rate caused by a low EM value. However, increasing the EM beyond the optimal value can lead to

Table 2
DSC results for neat PCL, neat TPU and developed UC blend.

Sample	T_m (°C)	T_g (°C)	T_c (C)	ΔH_m (J g^{-1})	X_c (%)
TPU	-	−43	-	-	-
30C70U	56	−43	35	15.71	37.67
PCL	58	−62	27	70.4	50.64

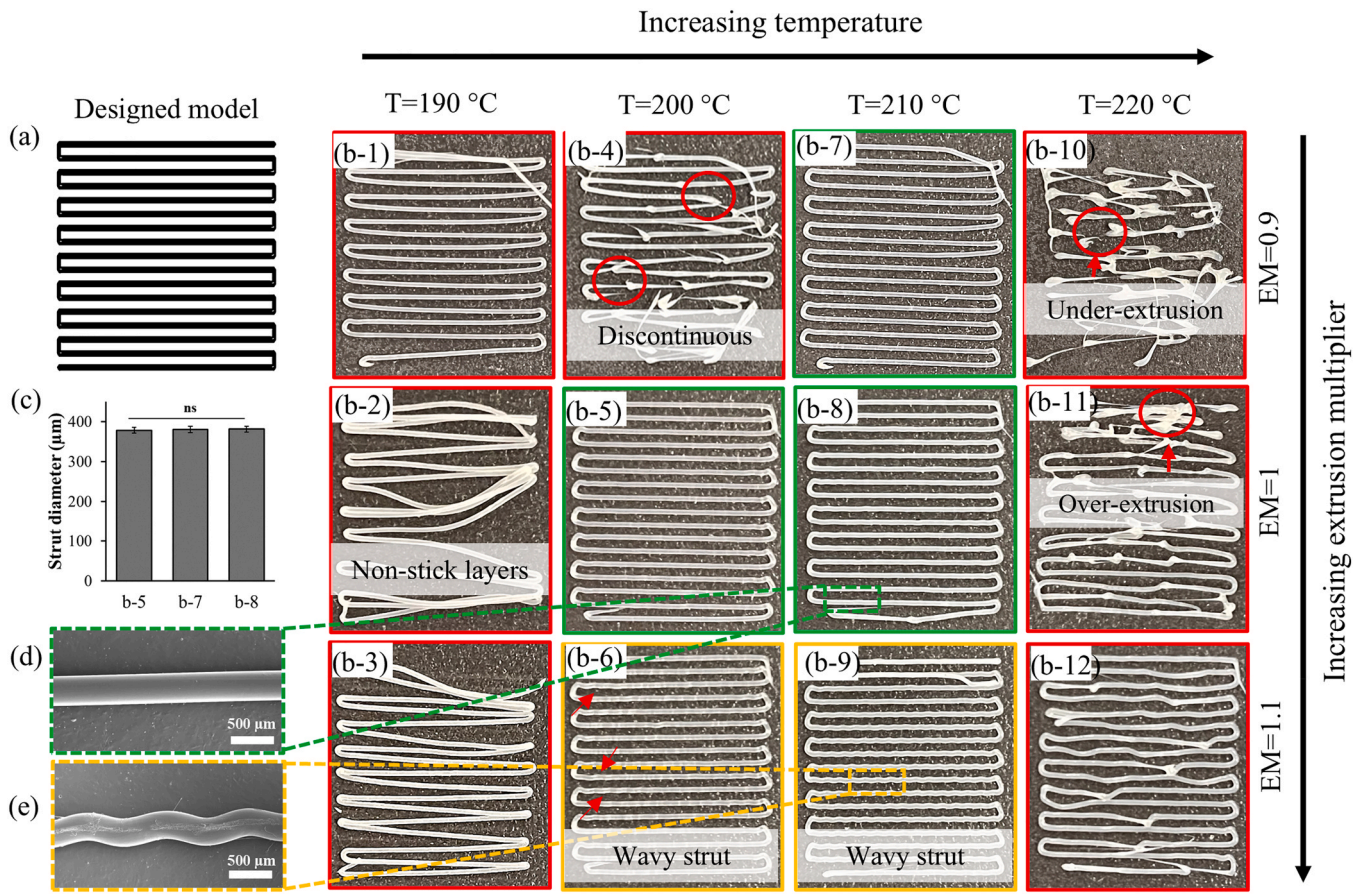

Fig. 5. Printability assessment of extruded filament. (a) CAD model of the design model, (b) light microscopy images of the FDM printed UC filament into parallelly arranged single lines. (c) Strut diameter achieved for 3D printed UC filament using nozzle temperature of 200°C and EM of 1 (b-5), nozzle temperature of 210°C and EM of 0.9 (b-7), and nozzle temperature of 210°C with EM= 1 (b-7), (d, e) SEM micrograph of the extruded filament using the same nozzle temperature of 210°C and different EM values of 1 and 1.1 respectively.

excessive material extrusion, resulting in defects such as over-extrusion, blobbing, and warping. Fig. 5b-11 and b-12 show that the printing temperature of 220°C combined with high EM levels led to the over extrusion and aggregated material problems. High printing temperature lowers the viscosity of the filament and negatively affects the filament's flow behavior [42]. The over-melted filament flows uncontrollably from the nozzle and promotes material inhomogeneity by the formation of aggregated material, thereby affecting the printed part's characteristics [31]. In summary, samples printed at 210°C with EM values of 0.9 and 1, and at 200°C with an EM of 1, demonstrated satisfactory quality, validating the appropriateness of the chosen EM and nozzle temperatures for high-quality sample printing. Notably, no statistically significant differences were observed in the strut diameter of 3D printed lines between nozzle temperatures of 200°C with EM of 1 and lines printed at 210°C with EM values of 0.9 and 1 (Fig. 5c).

It was observed that samples printed at 210°C with varied extrusion multiplier values met the criteria of good and acceptable quality marked by the green (Fig. 5b-7 and b-8) and yellow frames (Fig. 5b-9). Optimal results were achieved by maintaining EM= 1 at both 200°C and 210°C, leading to high-quality lines. Thus, a temperature of 210°C and an extrusion multiplier of 1 were designated as the optimum nozzle temperature and EM level. Fig. 5d provides a SEM image depicting the extruded strut under these optimized conditions.

3.3. Scaffold fabrication

The structure and architecture of scaffolds are pivotal factors in scaffold-based tissue engineering, as they play a significant role in determining the functionality and mechanical properties of the tissue-engineered scaffolds, and subsequently their potential applications in the healthcare industry [43]. We used the SEM technique to examine the scaffolds' microstructure, including the pore size, shape, distribution, and interconnectivity. Fig. 6 illustrates the 3D printed scaffolds and SEM images of their top surfaces, showcasing the porous structures of rectilinear, triangular, and gyroid designs with varying infill percentages. The SEM imaging results showed that all 3D printed scaffolds exhibited a uniform and interconnected pore distribution throughout their structure. Notably, all the designed scaffolds were fabricated with excellent structural integrity, without any impurities or cracks in their structure. In addition, the SEM imaging analysis also showed that the pore shapes of the scaffolds corresponded closely to the designed patterns. The rectilinear scaffolds had square pore shapes, the triangular scaffolds had triangular pore shapes, and the gyroid scaffolds had circular pore shapes, consistent with their respective design specifications.

Our analysis also revealed that the pore size of the FDM-printed scaffolds decreased as the infill percentage increased. This is because a higher infill percentage results in a smaller gap between the deposited filaments, leading to a denser scaffold structure with smaller pore sizes. Conversely, a lower infill percentage results in a larger gap between filaments, leading to a less dense structure with larger pore sizes (Fig. 6c and d). Furthermore, there was no significant difference ($P > 0.05$) in the pore size of the scaffolds fabricated using different patterns but with the same infill density. To support cell proliferation, differentiation, and tissue growth within a scaffold, it is essential to ensure that the structure possesses sufficiently high porosity and suitable pore size. Although porosities greater than 50 % are considered suitable for bone ingrowth

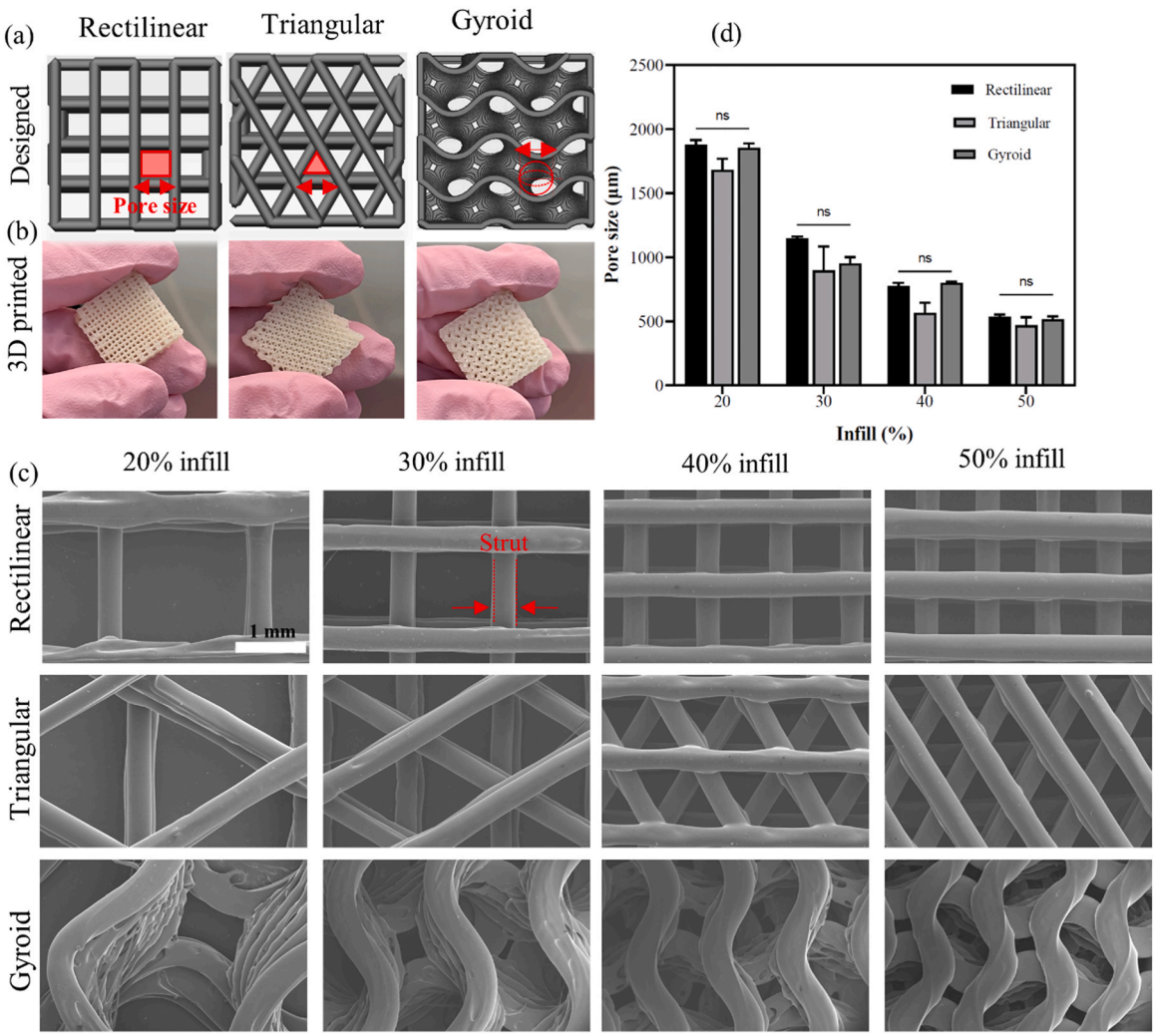

Fig. 6. (a) Computer aided design models of porous scaffolds, (b) actual FDM printed scaffolds fabricated based on rectilinear, triangular and gyroid designs using an infill density of 40 %, (c) macroscopic surface structures of the scaffolds with different filling densities and infill patterns, (d) Pore size analysis of FDM printed porous 3D scaffolds of rectilinear, triangular, and gyroid designs with different infill percentage.

in biomaterials, the optimal pore size for bone ingrowth is highly debated [44]. It has been recommended that scaffolds with pore sizes exceeding 300 µm are most effective for repairing large bone defects. Additionally, among different types of scaffolds, those with pore sizes ranging from 500 to 1200 µm have demonstrated excellent osteoinductive properties and sufficient vascularization of the tissue-engineered graft and successful bone regeneration. Pore sizes in this range provide ample space for the proliferation and differentiation of osteoblasts, as well as for extracellular matrix deposition, which are key processes in bone tissue formation. Furthermore, scaffolds with controlled pore sizes in this range offer a balance between mechanical stability and biological functionality, making them particularly suitable for large-area bone defect repair [45–48]. Our results indicate that scaffolds with infill densities of 30 %, 40 %, and 50 % for all designed patterns produced pores in the range of 500–1160 in size. In contrast, rectangular, triangular, and gyroid scaffolds with an infill density of 20 % had larger pore sizes, measuring 1860, 1770, and 1890, respectively. While larger pores may allow some degree of bone growth, they risk reduced osteogenesis due to lower surface area available for cell attachment and diminished scaffold mechanical integrity. Therefore, the pore size range of 500–1160 µm observed in our scaffolds with higher infill densities is well-suited for promoting successful bone regeneration, as supported by the cited literature.

3.4. Mechanical properties of UC scaffolds

One of the fundamental requirements for scaffolds is to possess adequate mechanical strength to withstand the stresses imposed on them during tissue growth and regeneration. The mechanical properties of scaffolds fabricated through FDM printing can be significantly influenced by the filament composition, infill pattern, and infill density used during printing [31]. Hence, producing scaffolds with mechanical properties similar to bone requires finding the right design and density for newly developed filament. The evaluation of compression properties of our 3D-printed UC scaffolds is shown in Fig. 7. All scaffolds were subjected to a total strain of 80 %, and the stress-strain curves for the scaffolds showed three stages. The initial phase, featuring linear behavior, signified the material's elastic response. Subsequently, a non-linear stress increase was observed as the material approached the plateau phase, reflecting the absence of failure and stretching of the struts. As compression continued, the material densified and its strength increased, as evidenced by the steepening of the slope of the stress-strain curve [49]. Fig. 7d shows images of the gyroid scaffold prior to and post compression testing. We did not observe any crack lines and any instances of brittle fracture in the scaffolds. The primary failure mechanism observed in all UC scaffolds was buckling, which can be attributed to the filament's composition, containing a high proportion of TPU. As a highly elastic material, TPU enables significant deformation under

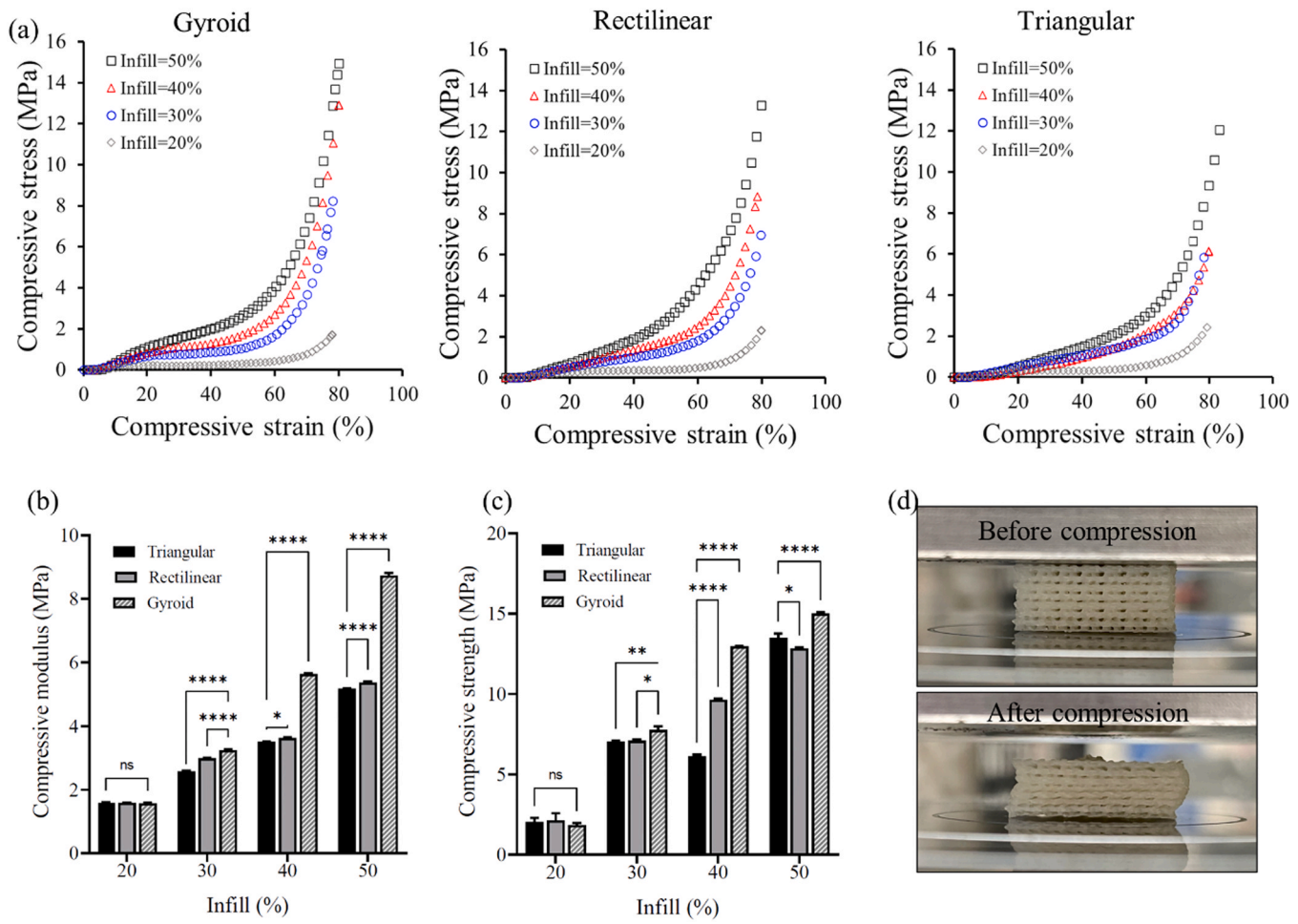

Fig. 7. (a) Stress-strain plots of the 3D-Printed Scaffolds of UC Blend with different pattern design and infill densities obtained by compression test, (b) FDM printed gyroid scaffolds printed using an infill percentage of 40 % before and after the compression test, (c,d) Compressive modulus and strength of FDM printed scaffolds. ns=not significant, *p < 0.05, * *p < 0.01, * **p < 0.001, * ** *p < 0.0001. Compression testing on scaffolds was conducted at room temperature.

compressive forces, leading to buckling rather than brittle fracture. XRD further supports this behavior by confirming the semi-crystalline structure of the UC filament, showcasing both crystalline PCL and amorphous TPU phases. The inclusion of TPU, as evidenced by broader and less intense crystalline peaks, reduces overall crystallinity and enhances elasticity—key factors influencing the scaffold's compressive response. This structure, characterized by a balanced blend of rigidity from PCL and flexibility from TPU, effectively minimizes brittle fracture and promotes buckling as the primary failure mode. The high elasticity and resilience of TPU within the amorphous phase allow the scaffold to deform extensively without fracturing, underscoring the suitability of this material blend for achieving the targeted mechanical performance in bone tissue engineering applications.

It was observed that densification occurred earlier in all patterns for scaffolds with higher infill density, which indicated a greater degree of elasticity. This finding suggests that such scaffolds are more resistant to compression, requiring more force to reach their maximum compressive strength. A comparison of scaffold designs revealed that, for scaffolds printed with the same infill densities, those with the gyroid pattern exhibit superior mechanical properties. The gyroid sample with 50 % infill had the highest modulus among the scaffolds, measuring at 8.75 MPa, while the gyroid with 40 % infill came in second place with an elastic modulus of 5.64 MPa (Fig. 7b). This is due to the gyroid's unique geometry, which provides better load-bearing capabilities and higher stiffness. The gyroid structure consists of a triply periodic minimal surface (TPMS) with interconnected channels and struts forming a continuous network, which allows for more uniform stress distribution compared to traditional designs like rectilinear and triangular patterns. The gyroid's smooth curvature minimizes stress concentrations that typically occur at sharp corners in rectilinear or triangular patterns, making the gyroid structure more resilient to deformation under compressive loads. This ability to distribute mechanical forces evenly across the scaffold significantly contributes to its higher modulus and load-bearing capacity. Moreover, the absence of abrupt transitions in the gyroid structure helps to reduce points of mechanical weakness, thus enhancing its resistance to deformation [49]. Spece et al. have also reported similar behavior for the mechanical properties of material extrusion-printed PEEK porous constructs based on gyroid and simple rectilinear design [44]. Another research study, which involved the comparison of SLS-printed strut-based lattices with different TPMS geometries, yielded similar results [50]. Following the gyroid design, rectilinear scaffolds displayed higher mechanical properties when compared to triangular scaffolds. The rectilinear scaffolds with 50 %, 40 %, and 30 % infill densities exhibited elastic modulus of 5.34, 3.61, and 2.99 MPa, respectively, whereas the corresponding values for triangular scaffolds were 5.16, 3.5, and 2.54 respectively. Previous studies have reported similar findings, indicating the impact of filament orientation on the stress distribution and elastic modulus of FDM printed. Specifically, scaffolds with aligned fiber orientation in the load direction demonstrate a more uniform stress distribution than those with non-aligned fibers [41,51,52]. However, for scaffolds with 20 % infill density, there was no statistically significant correlation found between

the compressive modulus/strength and infill pattern. The gyroid, triangular and rectilinear scaffolds with 20 % infill density exhibited the lowest compressive modulus of 1.55, 1.57, and 1.60 MPa, respectively.

Previous studies have reported compressive strength values for cancellous bone ranging from 1.5 to 45 MPa [53]. In our study, all developed scaffolds exhibited maximum compressive strength similar to natural bone ranging from 1.73 to 14.93 MPa for gyroid scaffolds with 20 % and 50 % infill densities, respectively. It is worth noting that maintaining scaffold shape in vitro requires a minimum compression modulus of 0.4 MPa [27], and we successfully developed scaffolds with a compressive modulus ranging from 1.55 to 8.75 MPa for scaffolds having 20 % and 50 % infill densities, correspondingly.

3.5. Shape memory performance of FDM printed scaffolds

The results from shape memory tests are illustrated in Fig. 8a to c.

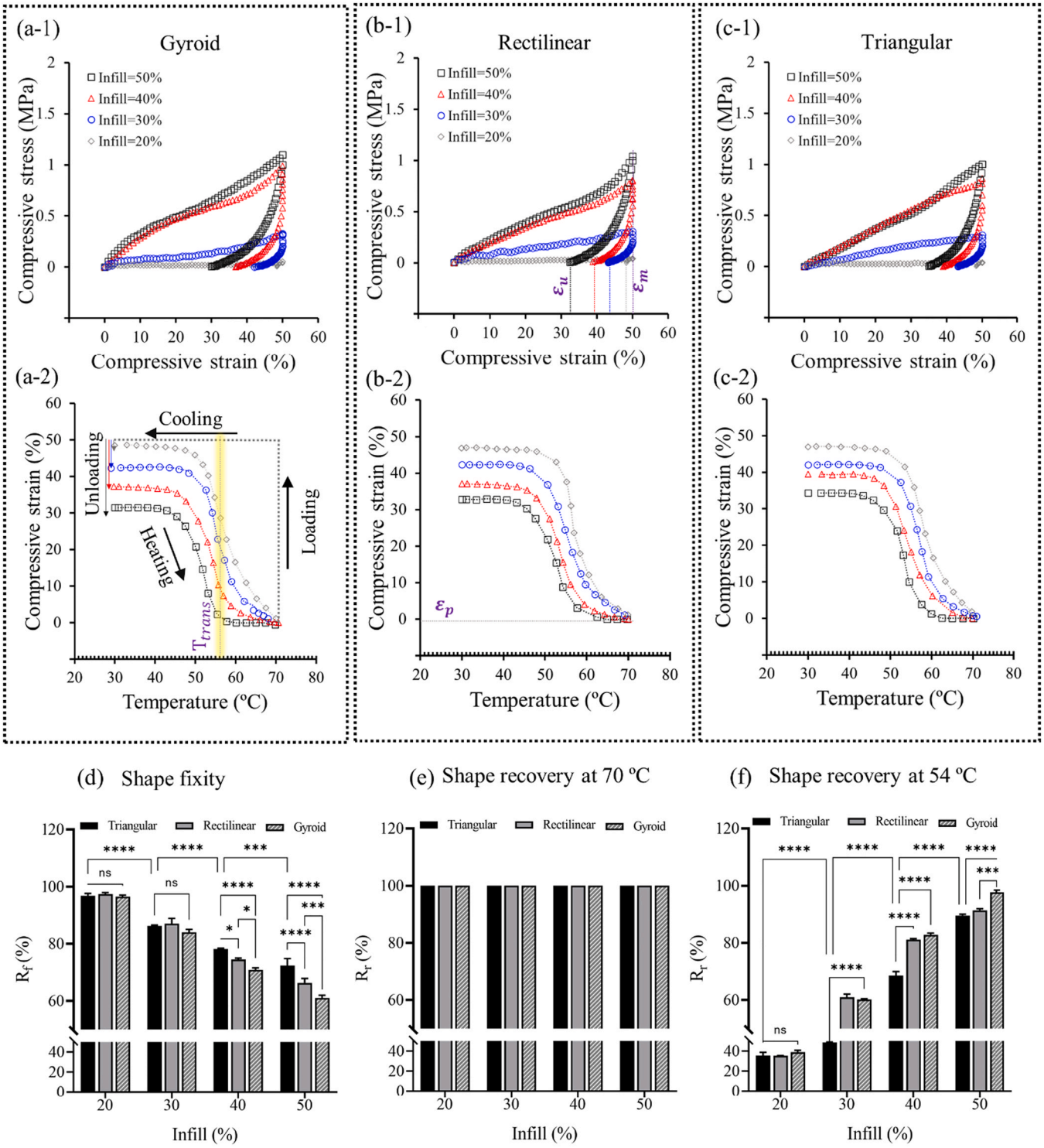

Fig. 8. (a, b, c) stress-strain and strain-temperature curves in the thermomechanical tests for gyroid, rectilinear, and triangular scaffolds, (d) Shape fixity ratio (R_f) of FDM printed scaffolds, (e) shape recovery ratio (R_r) of scaffolds at programming temperature 70°C, (f) shape recovery ratio (R_r) of scaffolds at transition temperature 56°C.

According to Eqs. 1 and 2, shape fixing, and shape recovery ratios were computed and graphically presented in Fig. 8e for all rectilinear, triangular and gyroid scaffolds, all subjected to compression up to a 50 % strain level. The shape memory behavior of these scaffolds is primarily governed by the interactions between the semi-crystalline PCL and the dominant amorphous TPU phases within the filament blend [27],[30], as evidenced by XRD and DSC analyses. XRD results confirmed the semi-crystalline nature of the UC filament, with distinct crystallization peaks at 21° and 24° associated with the PCL's (110) and (200) lattice planes. However, the intensity and sharpness of these peaks diminished with TPU's addition, suggesting reduced crystallinity. This reduction is significant as the crystalline regions of PCL play a vital role in shape fixity, where structural integrity is maintained during deformation, while the amorphous TPU phase allows for elasticity and energy storage during compression. DSC analysis further highlighted the thermal transitions critical to shape memory performance. The melting temperature of pure PCL was observed at 58°C, while the UC filament, with TPU incorporation, exhibited a reduced melting temperature of 52°C, indicative of lower crystallinity and a more flexible matrix. This temperature, representing the transition temperature (T_{trans}), enables programming of the temporary shape. When the material is deformed above T_{trans}, the PCL crystalline domains act as anchors, while the TPU matrix stores the elastic energy needed for recovery. Upon cooling below T_{trans}, the PCL segments crystallize, solidifying the temporary shape. When reheated above T_{trans}, the stored elastic energy within TPU is released, driving the scaffold back to its original shape. The elasticity and flexibility of the TPU phase are essential for enabling efficient shape recovery. This delicate interaction between the crystalline PCL segments and the amorphous TPU matrix is key to achieving both shape fixity and recovery. The shape memory behavior can be further tuned by adjusting the infill density and scaffold architecture, optimizing the balance between mechanical stability and recovery efficiency. Our study demonstrates that both infill pattern and density play crucial roles in determining the scaffold's ability to fix and recover its deformed shape.

When comparing scaffold designs printed with the same infill densities, it was found that the gyroid pattern exhibited lower shape fixity ability than the rectilinear design, followed by the triangular pattern. The shape fixity analysis, shown in Fig. 8d, revealed that for scaffolds printed with 50 % infill, the gyroid scaffold had the lowest shape fixity ratio, with an R_f value of 60 %. In contrast, the rectilinear design exhibited a higher shape fixity ratio, measuring at R_f= 66 %, while the triangular scaffolds showed even higher shape fixity, measuring at R_f= 70 %. This pattern was also observed in scaffolds printed with 40 % infill.

However, for infill densities of 20 % and 30 %, no significant difference was observed between the various infill patterns and their shape fixity ability. This suggests that, within a certain range of infill densities, the choice of infill pattern may not have a significant impact on the shape fixity ability of the 3D-printed object. It is possible that at lower infill densities, there is more empty space within the object, meaning that the infill material contributes less to the overall mechanical properties of the object. Therefore, the choice of infill pattern may have a smaller impact on the shape memory performance of 3D printed objects at higher porosities. A reverse correlation was also observed between infill percentage and shape fixity for all patterns. For instance, the triangular scaffolds demonstrated an R_f value of 96 %, 86 %, 78 %, and 70 % when printed with infill densities of 20 %, 30 %, 40 %, and 50 %, respectively.

The term shape fixity refers to how much an SMP-based structure is able to keep the temporary shape after removing the load. The shape fixity behavior can be attributed to the fact that scaffolds with higher densities also have higher elastic moduli and greater resistance to externally applied loads. As a result, they can withstand larger amounts of stress without permanent deformation, making it more difficult for the scaffold to fix the temporary shape when exposed to compression [54,55]. As mentioned earlier, the gyroid structure comprises a repeating pattern of interconnected channels and struts that form a TPMS. This unique network structure enhances structural interconnectivity, enabling the scaffold to withstand greater compressive loads while minimizing localized stress concentrations. As a result, the scaffold maintains its structural integrity even under deformation. Therefore, the relatively lower percentage of shape fixity observed in dense gyroid scaffolds may be attributed to their higher mechanical properties when compared to other scaffold designs. Mechanical testing results of rectilinear and triangular scaffolds printed with the same infill densities demonstrated that rectilinear scaffolds exhibited better compression properties compared to triangular scaffolds (Fig. 7b and c). This finding may explain the lower shape fixity observed for the rectilinear pattern in comparison to the triangular pattern.

While the scaffolds' pattern and infill density play a significant role in determining their fixity ability, interestingly, there was almost no impact of these factors on the value of shape recovery when subjected to their programming temperature. All scaffolds, regardless of their pattern or infill density, exhibited a full recovery of 100 % after being subjected to the temperature of 70°C.

However, the strain-temperature curves obtained from thermo-mechanical tests conducted on scaffolds with varying infill densities showed that the transition temperature moves to lower values as the infill density increases. For instance, in the case of gyroid scaffolds, those with 50 % and 40 % infill densities recovered the major stored strain at 52°C and 53°C respectively, while the values for those with 30 % and 20 % infill densities were 56°C and 58°C respectively. This can be attributed to the increased internal stress induced in the denser scaffolds, which enhances the ability to recover stored strain. Essentially, the internal stress and thermal energy-induced micro-Brownian motion work together to recover the strain at lower temperatures in the denser scaffolds [33]. This behavior underscores the importance of optimizing infill density for applications requiring rapid shape recovery at specific temperatures. Denser scaffolds not only exhibit better mechanical strength but also recover more efficiently at lower transition temperatures, which is crucial for minimally invasive medical applications where scaffold deployment needs to occur quickly and reliably.

Upon analyzing the strain-temperature curves and observing the strain recovery during the heating stage, it prompted another question: can the scaffolds fully recover their permanent shape when subjected to their transition temperature as effectively as they can recover their full shape at their programming temperature? To answer this question, the compressive strain of all scaffolds at transition temperature was recorded, and using Eq. 2, the shape recovery of developed scaffolds at their transition temperature was calculated (Fig. 8f).

Observations indicated that the scaffolds were incapable of entirely regaining their shape at the transition temperature. Nonetheless, it was found that increasing the infill percentage led to improved shape recovery of the scaffolds. Gyroid, rectilinear, and triangular scaffolds with 50 % infill exhibited recovery rates of 98 %, 91.1 %, and 89.5 %, respectively. Additionally, scaffolds printed with 40 % infill demonstrated good shape recovery, with all three patterns exhibiting values greater than 70 % (82.3 %, 80.9 %, and 70 % for gyroid, rectilinear, and triangular, respectively). In contrast, scaffolds printed with 30 % infill displayed lower recovery rates, ranging from 48 % to 60 %. Furthermore, scaffolds printed with 20 % infill demonstrated inadequate shape recovery, with values falling below 50 %.

These observations indicate that the shape memory behavior of the material is affected by temperature, with recovery values differing between the programming temperature (70°C) and the transition temperature (56°C). The transition temperature marks the point at which the material undergoes a phase change that allows it to recover its original shape. When the material is heated above this temperature, it undergoes a phase transition and the stored strain is released, allowing it to fully return to its original shape. Consequently, all scaffolds, regardless of their pattern and density, fully recover at the programming temperature. However, it's important to note that the shape recovery

process of all scaffolds isn't fully completed at the transition temperature alone. Additional heating above this threshold is necessary for complete stress relaxation and full restoration of the original shape [56]. Nevertheless, our findings emphasize that optimizing scaffold design and meticulously controlling process parameters result in superior shape recovery performance, even at the transition temperature. This is highlighted by the gyroid scaffold with 50 % infill density, which showcased the highest recovery ratio (98 %) at a transition temperature of 52°C compared to other scaffold patterns and densities, demonstrating exceptional performance even at this critical temperature.

Given that the transition temperature of the developed scaffolds exceeds body temperature, addressing this temperature gap can be achieved by safely elevating the temperature in a localized manner through external heating methods.

One potential approach to activate the developed scaffolds in vivo involves the use of hot saline irrigation during surgery. This method not only activates the compacted shape memory scaffold but also offers hemostatic benefits by accelerating clotting and reducing bleeding during and after surgery [57–59]. For example, Shehata et al. [58] reported that hot saline at 50°C improved surgical field quality and reduced blood loss during endoscopic sinus surgery. Similarly, Pfau et al. [59] demonstrated the use of hot saline to program and recover shape memory scaffolds with a transition temperature of 54°C in an in-vivo rat model, further highlighting its clinical applicability. Notably, the human body can tolerate brief periods of elevated temperatures, as evidenced by the clinical use of acrylic-based cements, where local temperatures can reach up to 70°C [60,61]. However, caution must be exercised, as Berman et al. [62] observed bone necrosis in rats exposed to temperatures exceeding 70°C. This underscores the importance of carefully managing temperature during scaffold activation. Fig. 9 illustrates the programming and recovery steps of a gyroid scaffold with 50 % infill density. The scaffold was heated in an environmental chamber to the programming temperature, loaded at a strain of 50 %, and then cooled to room temperature to obtain the temporary shape. The recovery process was performed in a lab oven to record and capture the scaffold's recovery performance at the transition temperature of 52°C. The results demonstrated that the scaffold was capable of regaining 98 % of its original shape in just 180 seconds when subjected to its transition temperature.

3.6. Wettability and cytocompatibility of un-treated and PDA treated UC scaffolds

Fig. 10a depicts a schematic illustration of the reaction mechanism and the PDA coating formation process used in the surface modification of FDM-printed UC scaffolds. To homogenously coat the polydopamine onto the scaffold's surface, the scaffold was immersed into a dopamine solution (tris buffer, pH=8.5) and stirred for 24 hours. During this process, PDA was developed through the self-polymerization of DA particles. The polydopamine coating was able to effectively form on both the surface and pore walls of the UC scaffold, as confirmed by optical and SEM imaging that demonstrated successful particle deposition (Fig. 10b and c). EDS mapping analysis also confirmed the presence of Nitrogen (N) as a significant component in the PDA-coated scaffold, as shown in Fig. 11a-2.

The morphology of MG-63 cells on both types of scaffolds was examined using SEM (Figs. 11a and b). The imaging results indicated that both scaffolds were suitable for cell attachment. However, cells on the PDA-coated scaffold exhibited better spreading, likely due to the hydrophilic properties conferred by the PDA particles, as confirmed by the water contact angle measurement presented in Fig. 11c. Untreated and PDA-treated scaffolds exhibited a contact angle of 88° and 56°, respectively. Polydopamine coatings have been identified to possess a high concentration of amine and hydroxyl functional groups; thus, they have been utilized to enhance the hydrophilicity of hydrophobic polymers. By modifying the surface with a polydopamine coating, it is possible to increase the surface energy of the material, which promotes greater wettability and encourages cellular adhesion and proliferation [28,33,35,36].

The result of cell proliferation by MTS assay presented in Fig. 11d confirms the biocompatibility of both uncoated and PDA-coated scaffolds toward MG-63 cells. Notably, on the seventh day of cell culture, a significant difference in proliferation was observed between the cells cultured on the PDA-coated scaffold compared to the uncoated sample. The absorption value increased from 0.82 nm for the uncoated scaffold to 1.67 nm for the PDA-coated scaffold, indicating that the PDA coating

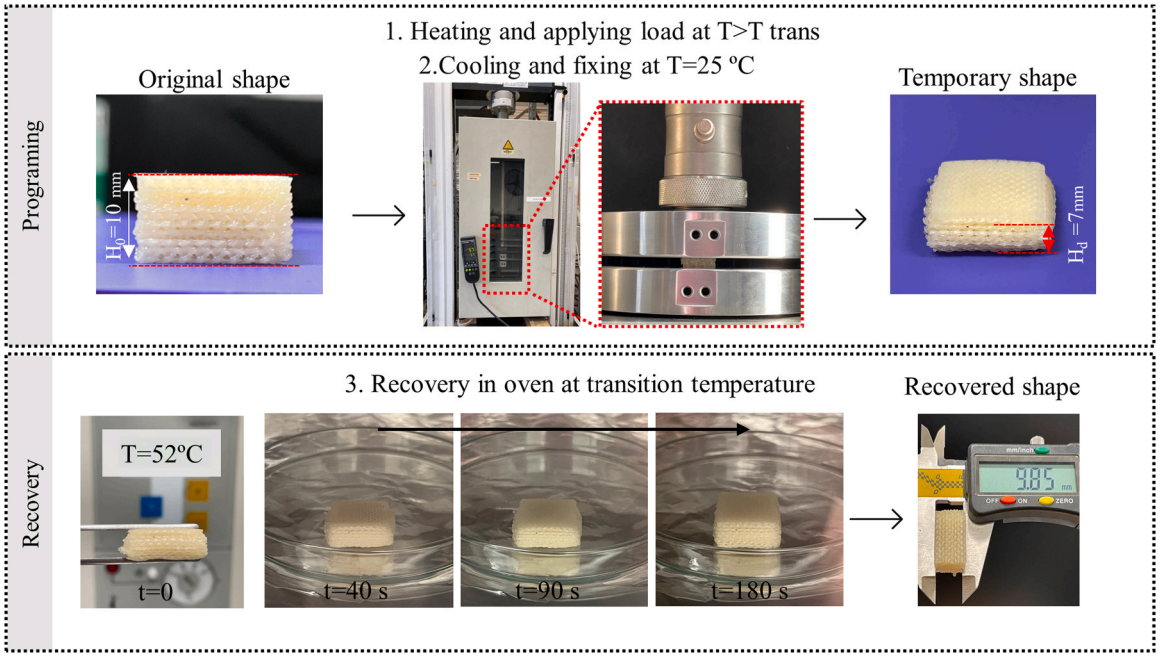

Fig. 9. The self-deploying potential of a gyroid scaffold with 50 % infill when subjected to the transition temperature of 52°C was evaluated. The scaffold exhibited 98 % recovery within a duration of only 180 seconds.

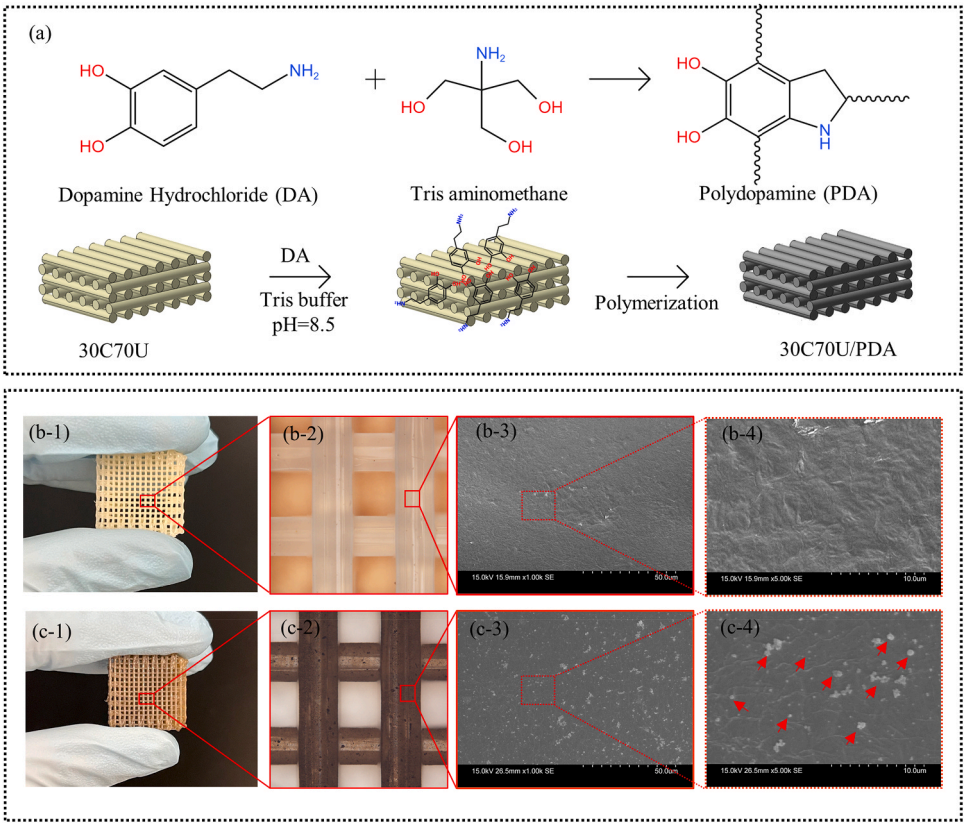

Fig. 10. (a) Schematic illustration of the polydopamine treatment process applied to a UC scaffold, (b and c) Optical and SEM images of unmodified and PDA-coated rectilinear scaffold 3d printed with a 40 % infill density. The dispersion of PDA particles is indicated by the red arrows in the image.

significantly enhanced cell proliferation. Qualitative analysis further revealed that the number of formed calcified nodules was higher on the PDA-coated scaffold than on the uncoated scaffold (marked with black arrows in Fig. 11a-1). Calcium nodules are a hallmark of osteoblast differentiation and are often used as a measure of bone formation in vitro. This observation can be attributed to the negatively charged functional groups of polydopamine coatings, which have been shown to induce apatite mineralization.

Furthermore, the EDS elemental mapping of both the untreated and PDA-coated scaffolds revealed the successful formation of a CaP biomineralized layer on their surfaces (Fig. 11a-2 and b-2). This was evidenced by the detection of calcium (Ca), Oxygen (O), carbon (C), and phosphorous (P). Importantly, the PDA-coated samples exhibited higher element density, indicating a more concentrated presence of these elements compared to the untreated samples. Consequently, the enhanced mineralization on the PDA-coated scaffold could provide a favorable environment for the osteogenic differentiation of Mg-63 cells and bone tissue regeneration [63].

Finally, the shape memory test performed on the PDA-coated scaffold (Fig. 11e) confirmed that the PDA coating did not compromise the scaffold's shape memory properties, underscoring the material's multifunctionality.

The shape memory feature enables the scaffold to recover its original complex structure upon activation, maximizing contact with the defect site and ensuring mechanical stability. This transformation not only provides mechanical support but also exposes a bioactive surface to the surrounding tissue. The PDA coating, with its hydrophilic and functional amine and hydroxyl groups, further enhances cellular adhesion, proliferation, and differentiation, thus accelerating early bone repair stages. The increased hydrophilicity, as evidenced by the reduced contact angle, directly supports cell attachment and spreading, while the bioactive surface promotes the deposition of calcium-phosphate mineral layers, as shown in our elemental mapping results. Furthermore, the PDA coating fosters an osteoinductive environment by creating a surface conducive to osteogenic signaling pathways. This bioactive surface, combined with the scaffold's dynamic adaptability, encourages cellular infiltration and nutrient exchange, potentially enhancing tissue ingrowth and vascularization. This interaction between scaffold mechanics and cellular bioactivity creates a favorable microenvironment that supports both initial cell attachment and long-term osteogenic differentiation and matrix formation.

The 4D-printed PDA-coated scaffold exemplifies a "bioactive smart" structure, combining shape memory functionality with enhanced bioactivity to address key challenges in bone tissue engineering. The shape memory feature ensures the scaffold recovers its original structure upon activation, enabling precise defect filling and providing mechanical stability while exposing a bioactive surface. The PDA coating, rich in hydrophilic and functional groups, significantly enhances cellular adhesion, proliferation, and differentiation, as evidenced by reduced contact angle, increased calcified nodule formation, and the deposition of calcium-phosphate biomineralized layers. Together, the dynamic adaptability of the scaffold and the bioactive surface foster a microenvironment conducive to early cell attachment, nutrient exchange, tissue ingrowth, and long-term osteogenic differentiation.

Future studies should explore the synergy between shape memory behavior and bioactive surface modifications by incorporating additional osteoinductive factors to further enhance regenerative performance. Investigating osteogenic differentiation through markers such as alkaline phosphatase (ALP) activity or osteocalcin expression will provide deeper insights into its biological potential. Moreover, long-term degradation studies under physiological conditions are essential to ensure controlled material dissolution, sustained mechanical integrity, and effective support for tissue regeneration. These investigations will bridge the gap between in vitro findings and in vivo applications,

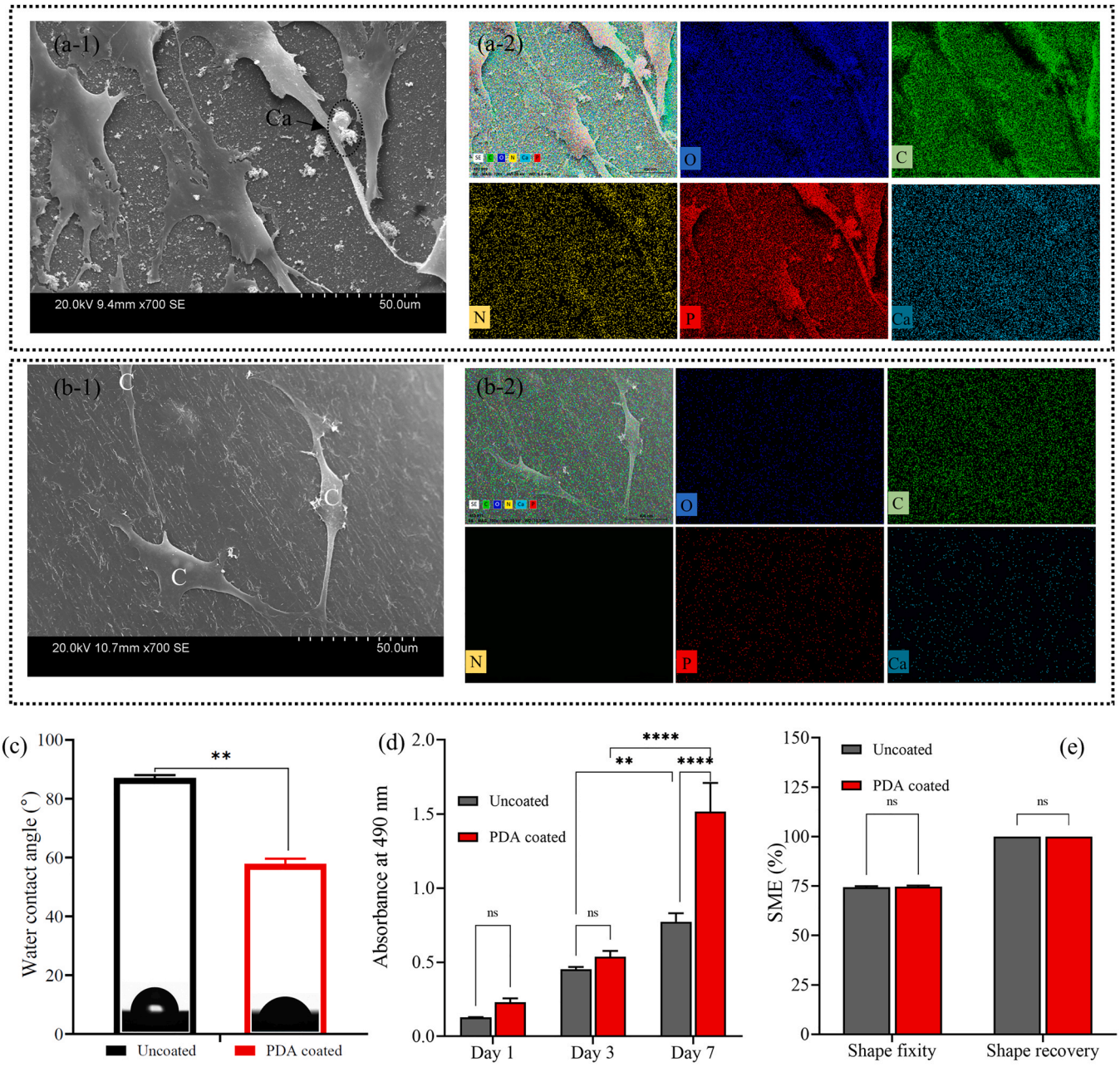

Fig. 11. (a-1 and b-1) SEM images depicting the morphology of MG-63 cells on PDA-coated and unmodified scaffolds, respectively. The presence of calcified nodules in PDA-coated scaffolds is highlighted by the black arrows in the image. (a-2 and b-2) Energy dispersive X-ray spectroscopy elemental mapping of PDA-coated and unmodified scaffolds, respectively. (c) Water contact angles of uncoated and PDA coated substrates, (d) The absorbance values of MTS assay of both uncoated and PDA coated scaffolds, and (e) Shape memory performance of scaffold before and after PDA coating.

strengthening the scaffold's preclinical evaluation and paving the way for clinical translation.

These future investigations would strengthen the scaffold's preclinical evaluation, ensuring its design aligns with the demands of in vivo applications. Overall, the PDA-coated scaffolds represent a promising advancement in bone tissue engineering, with their combined structural adaptability, bioactivity, and cytocompatibility addressing critical challenges in the field.

4. Conclusion

In conclusion, this study successfully developed a semicrystalline shape memory filament made of 70TPU/30PCL %wt., which was used for FDM 4D printing of porous scaffolds with tunable architecture, mechanical properties, and shape memory performance. An extensive evaluation has been carried out to characterize the influences of FDM printing parameters on the morphology, mechanical properties, and shape memory performance of the scaffolds. The SEM imaging results showed that all 3D printed scaffolds exhibited a uniform and interconnected pore distribution throughout their structure. Additionally, scaffolds printed with an infill density greater than 30 % displayed pore sizes that are considered suitable for bone regeneration. The mechanical testing analysis revealed that the gyroid pattern scaffold exhibited the highest mechanical properties, followed by the rectilinear pattern and then the triangular pattern. Furthermore, all 3D printed scaffolds using the developed smart filament displayed maximum compressive strength comparable to that of natural spongy bone, ranging from 1.73 to 14.93 MPa. Thermomechanical cyclic tests demonstrated the potential

for tailoring the shape fixity, shape recovery, and recovery temperature of programmed scaffolds by manipulating infill patterns and density parameters in FDM printing, directly affecting the stored strain and internal stress generated within the scaffolds during programming and recovery steps. Scaffolds with a gyroid, rectilinear, and triangular infill pattern and 50 % infill density exhibited the highest shape recovery performance at the transition temperature of 52°C, with shape recovery percentages of 98 %, 91.1 %, and 89.5 %, respectively. Our results showed that the shape memory properties of the scaffold were not affected by the polydopamine coating. However, the coating significantly enhanced both the hydrophilicity of the scaffold and cell proliferation levels. Overall, this study's findings offer a promising direction for designing and fabricating porous shape memory scaffolds with adjustable mechanical strength and shape memory performance for potential applications in the customized treatment of irregular bone defect regeneration.

CRediT authorship contribution statement

Nasim Sabahi: Writing – original draft, Visualization, Methodology, Investigation, Formal analysis, Data curation, Conceptualization. **Iman Roohani:** Writing – review & editing, Supervision. **Chun H. Wang:** Writing – review & editing, Supervision. **Xiaopeng Li:** Writing – review & editing, Supervision, Funding acquisition.

Declaration of Competing Interest

The authors declare that they have no known competing financial interests or personal relationships that could have appeared to influence the work reported in this paper.

Acknowledgements

X.L. is the recipient of a Discovery Early Career Researcher Award (DE190101495). The authors are grateful for the scientific and technical support, as well as the facilities provided by the UNSW Mark Wainwright Analytical Centre (MWAC).

Appendix A. Supporting information

Supplementary data associated with this article can be found in the online version at doi:10.1016/j.addma.2024.104636.

Data availability

Data will be made available on request.

References

[1] G.N. Duda, S. Geissler, S. Checa, S. Tsitsilonis, A. Petersen, K. Schmidt-Bleek, The decisive early phase of bone regeneration, Nat. Rev. Rheumatol. 19 (2) (2023) 78–95, https://doi.org/10.1038/s41584-022-00887-0.
[2] F. Migliorini, G. La Padula, E. Torsiello, F. Spiezia, F. Oliva, N. Maffulli, Strategies for large bone defect reconstruction after trauma, infections or tumour excision: a comprehensive review of the literature, Eur. J. Med. Res. 26 (1) (2021) 1–10, https://doi.org/10.1186/s40001-021-00593-9.
[3] L. Wang, et al., Smart, elastic, and nanofiber-based 3D scaffolds with self-deploying capability for osteoporotic bone regeneration, Nano Lett. 19 (12) (2019) 9112–9120, https://doi.org/10.1021/acs.nanolett.9b04313.
[4] Y. Xu, F. Zhang, W. Zhai, S. Cheng, J. Li, Y. Wang, Unraveling of advances in 3D-printed polymer-based bone scaffolds, Polymers 14 (3) (2022), https://doi.org/10.3390/polym14030566.
[5] R. Xue, et al., DLP printing of BT/HA nanocomposite ceramic scaffolds using low refractive index BT crystals, J. Mater. 10 (5) (2024) 1036–1048, https://doi.org/10.1016/j.jmat.2023.11.004.
[6] X. Zhang, et al., Four-dimensional printing and shape memory materials in bone tissue engineering, Int. J. Mol. Sci. 24 (1) (2023), https://doi.org/10.3390/ijms24010814.
[7] X. Chen, et al., Harnessing 4D printing bioscaffolds for advanced orthopedics, Small 18 (36) (2022) 1–19, https://doi.org/10.1002/smll.202106824.
[8] M.R. Pfau, M.A. Grunlan, Smart scaffolds: shape memory polymers (SMPs) in tissue engineering, J. Mater. Chem. B 9 (21) (2021) 4287–4297, https://doi.org/10.1039/d1tb00607j.
[9] N. Sabahi, W. Chen, C.H. Wang, J.J. Kruzic, X. Li, A review on additive manufacturing of shape-memory materials for biomedical applications, Jom 72 (3) (2020) 1229–1253, https://doi.org/10.1007/s11837-020-04013-x.
[10] E.J. Shin, Y.S. Jung, C.H. Park, S. Lee, Eco-friendly TPU/PLA blends for application as shape-memory 3D printing filaments, J. Polym. Environ. (0123456789) (2023), https://doi.org/10.1007/s10924-023-02799-w.
[11] M. Carlson, Y. Li, Development and kinetic evaluation of a low-cost temperature-sensitive shape memory polymer for 4-dimensional printing, Int. J. Adv. Manuf. Technol. 106 (9–10) (2020) 4263–4279, https://doi.org/10.1007/s00170-020-04927-5.
[12] Y. Wang, et al., Effects of the composition ratio on the properties of PCL/PLA blends: a kind of thermo-sensitive shape memory polymer composites, J. Polym. Res. 28 (12) (2021) 1–13, https://doi.org/10.1007/s10965-021-02815-4.
[13] Y. Wang, J. Zhang, M. Li, M. Lei, Y. Wang, Q. Wei, 3D printing thermo-responsive shape memory polymer composite based on PCL/TPU blends, J. Polym. Res. 29 (6) (2022) 1–14, https://doi.org/10.1007/s10965-022-03095-2.
[14] D. Rahmatabadi, et al., Toughening PVC with biocompatible PCL softeners for supreme mechanical properties, morphology, shape memory effects, and FFF printability, Macromol. Mater. Eng. 308 (10) (2023), https://doi.org/10.1002/mame.202300114.
[15] C. Lin, L. Liu, Y. Liu, J. Leng, 4D printing of shape memory polybutylene succinate/polylactic acid (PBS/PLA) and its potential applications, Compos. Struct. 279 (July 2021) (2022) 114729, https://doi.org/10.1016/j.compstruct.2021.114729.
[16] F. Zhang, L. Wang, Z. Zheng, Y. Liu, J. Leng, Magnetic programming of 4D printed shape memory composite structures, Compos. Part A Appl. Sci. Manuf. 125 (April) (2019) 105571, https://doi.org/10.1016/j.compositesa.2019.105571.
[17] S.T. Ly, J.Y. Kim, 4D printing – fused deposition modeling printing with thermal-responsive shape memory polymers, Int. J. Precis. Eng. Manuf. Green. Technol. 4 (3) (2017) 267–272, https://doi.org/10.1007/s40684-017-0032-z.
[18] Y. Liu, et al., Microstructural design for enhanced shape memory behavior of 4D printed composites based on carbon nanotube/polylactic acid filament, Compos. Sci. Technol. 181 (January) (2019), https://doi.org/10.1016/j.compscitech.2019.107692.
[19] F.S. Senatov, et al., Shape memory effect in 3D-printed scaffolds for self-fitting implants, Eur. Polym. J. 93 (2017) 222–231, https://doi.org/10.1016/j.eurpolymj.2017.06.011.
[20] F.S. Senatov, K.V. Niaza, M.Y. Zadorozhnyy, A.V. Maksimkin, S.D. Kaloshkin, Y. Z. Estrin, Mechanical properties and shape memory effect of 3D-printed PLA-based porous scaffolds, J. Mech. Behav. Biomed. Mater. 57 (2016) 139–148, https://doi.org/10.1016/j.jmbbm.2015.11.036.
[21] F.S. Senatov, K.V. Niaza, A.A. Stepashkin, S.D. Kaloshkin, Low-cycle fatigue behavior of 3d-printed PLA-based porous scaffolds, Compos. Part B Eng. 97 (2016) 193–200, https://doi.org/10.1016/j.compositesb.2016.04.067.
[22] A.B. Kutikov, K.A. Reyer, J. Song, Shape-memory performance of thermoplastic amphiphilic triblock copolymer poly(D,L-lactic acid-co-ethylene glycol-co-D,L-lactic acid) (PELA)/hydroxyapatite composites, Macromol. Chem. Phys. 215 (24) (2014) 2482–2490, https://doi.org/10.1002/macp.201400340.
[23] W. Zhou, X. Dong, Y. He, W. Zheng, J. Leng, In-vitro and in-vivo studies of 4D printed shape memory scaffolds with bioactive fillers and coating for enhanced bone tissue regeneration, Smart Mater. Struct. 31 (10) (2022), https://doi.org/10.1088/1361-665X/ac884a.
[24] M.A. Yousefi, D. Rahmatabadi, M. Baniassadi, M. Bodaghi, M. Baghani, 4D Printing of multifunctional and biodegradable PLA-PBAT-Fe3O4 nanocomposites with supreme mechanical and shape memory properties, Macromol. Rapid Commun. 2400661 (2024) 1–18, https://doi.org/10.1002/marc.202400661.
[25] T. Distler, et al., Polymer-bioactive glass composite filaments for 3D scaffold manufacturing by fused deposition modeling: fabrication and characterization, Front. Bioeng. Biotechnol. 8 (2020) 1–17, https://doi.org/10.3389/fbioe.2020.00552.
[26] X. Jing, H.Y. Mi, H.X. Huang, L.S. Turng, Shape memory thermoplastic polyurethane (TPU)/poly(ε-caprolactone) (PCL) blends as self-knotting sutures, J. Mech. Behav. Biomed. Mater. 64 (2016) 94–103, https://doi.org/10.1016/j.jmbbm.2016.07.023.
[27] N. Sabahi, I. Roohani, C.H. Wang, E. Farajzadeh, X. Li, Thermoplastic polyurethane-based shape memory polymers with potential biomedical application: the effect of TPU soft-segment on shape memory effect and cytocompatibility, Polymers 283 (2023) 126189, https://doi.org/10.1016/j.polymer.2023.126189.
[28] R. Baptista, M. Guedes, Porosity and pore design influence on fatigue behavior of 3D printed scaffolds for trabecular bone replacement, J. Mech. Behav. Biomed. Mater. 117 (2021) 104378, https://doi.org/10.1016/j.jmbbm.2021.104378.
[29] N. Sabahi, E. Farajzadeh, I. Roohani, C.H. Wang, X. Li, Material extrusion 3D printing of polyether-ether-ketone scaffolds based on triply periodic minimal surface designs: a numerical and experimental investigation, Appl. Mater. Today 39 (2024) 102262, https://doi.org/10.1016/j.apmt.2024.102262.
[30] B. Tandon, et al., Performance comparison of shape memory polymer structures printed by fused deposition modeling and melt electrowriting, Adv. Mater. Technol. 2400466 (2024) 1–12, https://doi.org/10.1002/admt.202400466.
[31] I.J. Solomon, P. Sevvel, J. Gunasekaran, A review on the various processing parameters in FDM, Mater. Today Proc. 37 (Part 2) (2020) 509–514, https://doi.org/10.1016/j.matpr.2020.05.484.

[32] B. Atli, F. Gandhi, G. Karst, Thermomechanical characterization of shape memory polymers, J. Intell. Mater. Syst. Struct. 20 (1) (2009) 87–95, https://doi.org/10.1177/1045389X07086689.
[33] H. Tobushi, D. Shimada, S. Hayashi, M. Endo, Shape fixity and shape recovery of polyurethane shape-memory polymer foams, Proc. Inst. Mech. Eng. Part L J. Mater. Des. Appl. 217 (2) (2003) 135–143, https://doi.org/10.1243/146442003321673635.
[34] A. Vayyaprontavida Kaliyathan, K.M. Varghese, A.S. Nair, S. Thomas, Rubber–rubber blends: a critical review, Prog. Rubber, Plast. Recycl. Technol. 36 (3) (2020) 196–242, https://doi.org/10.1177/1477760619895002.
[35] R. Han, et al., 3D printing-enabled self-assembling β-nucleating agent alignment: Structural evolution and mechanical performances, Polymers 246 (2022) 124736, https://doi.org/10.1016/j.polymer.2022.124736.
[36] S. Gantenbein, K. Masania, W. Woigk, J.P.W. Sesseg, T.A. Tervoort, A.R. Studart, Three-dimensional printing of hierarchical liquid-crystal-polymer structures, Nature 561 (7722) (2018) 226–230, https://doi.org/10.1038/s41586-018-0474-7.
[37] Ş. Poyraz, Z. Altınışık, A.S. Çakmak, M. Şimşek, M. Gümüşderelioğlu, Random/aligned electrospun PCL fibrous matrices with modified surface textures: characterization and interactions with dermal fibroblasts and keratinocytes, Colloids Surf. B Biointerfaces 218 (July) (2022), https://doi.org/10.1016/j.colsurfb.2022.112724.
[38] Z. Jiang, B. Diggle, M.L. Tan, J. Viktorova, C.W. Bennett, L.A. Connal, Extrusion 3D printing of polymeric materials with advanced properties, Adv. Sci. 7 (17) (2020) 1–32, https://doi.org/10.1002/advs.202001379.
[39] P. Geng, et al., Effects of extrusion speed and printing speed on the 3D printing stability of extruded PEEK filament, J. Manuf. Process. 37 (2018) (2019) 266–273, https://doi.org/10.1016/j.jmapro.2018.11.023.
[40] R.F. Quero, G. Domingos Da Silveira, J.A. Fracassi Da Silva, D.P. De Jesus, Understanding and improving FDM 3D printing to fabricate high-resolution and optically transparent microfluidic devices, Lab Chip 21 (19) (2021) 3715–3729, https://doi.org/10.1039/d1lc00518a.
[41] M. Doshi, A. Mahale, S.K. Singh, S. Deshmukh, Printing parameters and materials affecting mechanical properties of FDM-3D printed Parts: perspective and prospects, Mater. Today Proc. 50 (2021) 2269–2275, https://doi.org/10.1016/j.matpr.2021.10.003.
[42] P. Chen, et al., Recent advances on high-performance polyaryletherketone materials for additive manufacturing, Adv. Mater. (2022) 2200750, https://doi.org/10.1002/adma.202200750.
[43] S.T. Ho, D.W. Hutmacher, A comparison of micro CT with other techniques used in the characterization of scaffolds, Biomaterials 27 (8) (2006) 1362–1376, https://doi.org/10.1016/j.biomaterials.2005.08.035.
[44] H. Spece, T. Yu, A.W. Law, M. Marcolongo, S.M. Kurtz, 3D printed porous PEEK created via fused filament fabrication for osteoconductive orthopaedic surfaces, J. Mech. Behav. Biomed. Mater. 109 (2020), https://doi.org/10.1016/j.jmbbm.2020.103850.
[45] A.R. Amini, D.J. Adams, C.T. Laurencin, S.P. Nukavarapu, Optimally porous and biomechanically compatible scaffolds for large-area bone regeneration, Tissue Eng. Part A 18 (13–14) (2012) 1376–1388, https://doi.org/10.1089/ten.tea.2011.0076.
[46] D.J. Lee, et al., Effect of pore size in bone regeneration using polydopamine-laced hydroxyapatite collagen calcium silicate scaffolds fabricated by 3D mould printing technology, Orthod. Craniofacial Res. 22 (S1) (2019) 127–133, https://doi.org/10.1111/ocr.12261.
[47] C. Ghayor, F.E. Weber, Osteoconductive microarchitecture of bone substitutes for bone regeneration revisited, Front. Physiol. 9 (2018) 1–10, https://doi.org/10.3389/fphys.2018.00960.
[48] D.W. Hutmacher, J.T. Schantz, C.X.F. Lam, K.C. Tan, T.C. Lim, State of the art and future directions of scaffold-based bone engineering from a biomaterials perspective, J. Tissue Eng. Regen. Med. 1 (4) (2007) 245–260, https://doi.org/10.1002/term.24.
[49] A. Rege, Constitutive modeling of the densification behavior in open-porous cellular solids, Materials 14 (11) (2021) 1–10, https://doi.org/10.3390/ma14112731.
[50] O. Al-Ketan, R. Rowshan, R.K. Abu Al-Rub, Topology-mechanical property relationship of 3D printed strut, skeletal, and sheet based periodic metallic cellular materials, Addit. Manuf. 19 (2018) 167–183, https://doi.org/10.1016/j.addma.2017.12.006.
[51] Z. Zhao, F. Peng, K.A. Cavicchi, M. Cakmak, R.A. Weiss, B.D. Vogt, Three-dimensional printed shape memory objects based on an olefin ionomer of zinc-neutralized poly(ethylene-co-methacrylic acid), ACS Appl. Mater. Interfaces 9 (32) (2017) 27239–27249, https://doi.org/10.1021/acsami.7b07816.
[52] H. Liu, et al., Effects of fiber cross-angle structures on the mechanical property of 3D printed scaffolds and performance of seeded MC3T3-E1 cells, ACS Omega 6 (49) (2021) 33665–33675, https://doi.org/10.1021/acsomega.1c04672.
[53] P. Jb. Sl. D, Bone Repair Biomaterials. Elsevier Inc. [Online]. Available: ⟨10.1533/9781845696610⟩.
[54] A. Pirhaji, E. Jebellat, N. Roudbarian, K. Mohammadi, M.R. Movahhedy, M. Asle Zaeem, Large deformation of shape-memory polymer-based lattice metamaterials, Int. J. Mech. Sci. 232 (2022), https://doi.org/10.1016/j.ijmecsci.2022.107593.
[55] G. Le Fer, M.L. Becker, 4D printing of resorbable complex shape-memory poly (propylene fumarate) star scaffolds, ACS Appl. Mater. Interfaces 12 (20) (2020) 22444–22452, https://doi.org/10.1021/acsami.0c01444.
[56] Y.C. Sun, B.D. Leaker, J.E. Lee, R. Nam, H.E. Naguib, Shape programming of polymeric based electrothermal actuator (ETA) via artificially induced stress relaxation, Sci. Rep. 9 (1) (2019) 1–12, https://doi.org/10.1038/s41598-019-47949-0.
[57] D. Nagarajah, Y.C. Kueh, N.M. Lazim, B. Abdullah, The hemostatic effect of hot saline irrigation in endoscopic sinus surgery: a systematic review and meta-analysis, Syst. Rev. 11 (1) (2022) 1–10, https://doi.org/10.1186/s13643-022-02113-0.
[58] A. Shehata, M.S. Ibrahim, M.H. Abd-El-Fattah, Topical tranexamic acid versus hot saline for field quality during endoscopic sinus surgery, Egypt. J. Otolaryngol. 30 (4) (2014) 327–331, https://doi.org/10.4103/1012-5574.144965.
[59] M.R. Pfau, et al., Evaluation of a self-fitting, shape memory polymer scaffold in a rabbit calvarial defect model, Acta Biomater. 136 (2021) 233–242, https://doi.org/10.1016/j.actbio.2021.09.041.
[60] M. Stańczyk, B. Van Rietbergen, Thermal analysis of bone cement polymerisation at the cement-bone interface, J. Biomech. 37 (12) (2004) 1803–1810, https://doi.org/10.1016/j.jbiomech.2004.03.002.
[61] S.B. Kim, et al., The characteristics of a hydroxyapatite-chitosan-PMMA bone cement, Biomaterials 25 (26) (2004) 5715–5723, https://doi.org/10.1016/j.biomaterials.2004.01.022.
[62] A.T. Berman, J.S. Reid, D.R. Yanicko, G.C. Sih, M.R. Zimmerman, Thermally induced bone necrosis in rabbits. Relation to implant failure in humans, Clin. Orthop. Relat. Res. 186 (1984) 284–292.
[63] H. Lee, S.M. Dellatore, W.M. Miller, P.B. Messersmith, 2008, Polydopamine Coating," Science (80-.)., vol. 318, no. 5849, pp. 426–430, 2008, doi: 10.1126/science.1147241.Mussel-Inspired.